The Astrophysical Journal Supplement Series, 170:152–174, 2007 May

A SEARCH FOR FORMALDEHYDE 6 cm EMISSION TOWARD YOUNG STELLAR OBJECTS. II. H_2CO AND H110α OBSERVATIONS

E. Araya,[1,2] P. Hofner,[1,2] W. M. Goss,[2] H. Linz,[3] S. Kurtz,[4] and L. Olmi[5,6]

Received 2006 December 30; accepted 2007 February 7

ABSTRACT

We report the results of our second survey for Galactic H_2CO maser emission toward young stellar objects. Using the GBT and the VLA in the A configuration we observed 58 star-forming regions and discovered the fifth H_2CO 6 cm maser region in the Galaxy (G23.71−0.20). We have discussed the detection toward G23.71−0.20 in a previous paper. Here we present all the other results from our survey, including detection of H_2CO absorption features toward 48 sources, detection of the H110α recombination line toward 29 sources, detection (including tentative detections) of the carbon recombination line C110α toward 14 sources, subarcsecond angular resolution images of 6 cm continuum emission toward five sources, and observations of the H_2CO masers in IRAS 18566+0408 and NGC 7538. In the case of NGC 7538, we detected the two main H_2CO maser components, and our observations confirm variability of the blueshifted component recently reported by Hoffman et al. The variability of both maser components in NGC 7538 could be caused by a shock wave that reached the redshifted component approximately 14 yr before reaching the blueshifted component. If that were the case, we would expect to detect an increase in the flux density rate of change of the blueshifted component sometime after the year 2009. Our data also support the use of H_2CO/H110α observations as a tool to resolve the kinematic distance ambiguity of massive star-forming regions in the Galaxy.

Subject headings: H II regions — ISM: clouds — ISM: molecules — radio lines: ISM — stars: formation

1. INTRODUCTION

Formaldehyde (H_2CO) was discovered in the interstellar medium by Snyder et al. (1969) via observations of the 6 cm H_2CO *K*-doublet transition. The H_2CO 6 cm line is commonly detected in *absorption* toward molecular clouds in the Galaxy (e.g., Downes et al. 1980; Young et al. 2004), whereas H_2CO 6 cm *emission* is a far less common phenomenon. The H_2CO 6 cm line has been detected as thermal emission only toward the Orion BN-KL Nebula (Zuckerman et al. 1975; see also discussion in Araya et al. 2006b), confirmed as megamaser emission toward three extragalactic objects (Araya et al. 2004a), and, before this survey, found as maser emission toward four Galactic regions: NGC 7538, Sgr B2, G29.96−0.02, and IRAS 18566+0408 (Downes & Wilson 1974; Whiteoak & Gardner 1983; Pratap et al. 1994; Araya et al. 2005b, respectively).

H_2CO 6 cm masers seem to exclusively pinpoint very young regions of massive star formation (e.g., Araya et al. 2006a), and their rarity may be the consequence of short-lived physical conditions close to young massive stellar objects. However, the physical conditions and pumping mechanism that lead to H_2CO 6 cm masers are uncertain (e.g., Hoffman et al. 2003). A larger sample of H_2CO maser regions is necessary to constrain theoretical models for H_2CO maser emission and to assess whether H_2CO 6 cm masers are only found close to massive young stellar objects (within a few thousand AU), or whether they can be found at larger distances as Class I CH_3OH masers (e.g., Kurtz et al. 2004).

In this paper we report the results of the most extensive survey specifically focused on the search for H_2CO 6 cm Galactic masers. The observations were conducted with the Green Bank Telescope and the Very Large Array. This work is the continuation of our Arecibo survey for H_2CO emission toward young stellar objects (Araya et al. 2004b, hereafter Paper I). The main result of the present work is the detection of H_2CO maser emission in G23.71−0.20, previously reported by Araya et al. (2006a). Here we report the details of the survey that led to the detection of H_2CO maser emission in G23.71−0.20. This paper has the goal of making available to the community a data set of H_2CO 6 cm absorption and radio recombination lines (RRLs). The data reported in this work should prove useful for future studies of the regions included in our survey and for statistical studies of molecular clouds and H II regions in the Galaxy.

2. OBSERVATIONS

We observed 58 Galactic star-forming regions to search for H_2CO 6 cm emission; 48 sources were observed with the Green Bank Telescope (GBT), and 10 were observed with the Very Large Array (VLA)[7] in the A configuration. In Table 1 we list the observed sources. The selection criteria, details of the observations, and data reduction procedure are discussed below.

2.1. *GBT Observations*

Primarily (as in the case of our Arecibo survey, Paper I) we selected sources without strong centimeter radio continuum ($\lesssim$100 mJy)[8] in order to avoid as much as possible H_2CO 6 cm

[1] New Mexico Institute of Mining and Technology, Physics Department, Socorro, NM 87801.
[2] National Radio Astronomy Observatory, Socorro, NM 87801.
[3] Max-Planck-Institut für Astronomie, D-69117 Heidelberg, Germany.
[4] Centro de Radioastronomía y Astrofísica, Universidad Nacional Autónoma de México, 58089 Morelia, Michoacán, Mexico.
[5] Istituto di Radioastronomia, INAF, Sezione di Firenze, I-50125 Florence, Italy.
[6] University of Puerto Rico at Rio Piedras, Physics Department, P.O. Box 23343, San Juan, PR 00931.

[7] The 100 m Green Bank Telescope (GBT) and the Very Large Array (VLA) are operated by the National Radio Astronomy Observatory (NRAO), a facility of the National Science Foundation operated under cooperative agreement by Associated Universities, Inc.

[8] We prefer not to report the radio continuum flux densities from the literature because no uniform database was used for the source selection; i.e., the measurements are of a very heterogeneous nature, with differences in technique and aperture from source to source.

TABLE 1

OBSERVED SOURCES

Source	α(2000.0)	δ(2000.0)	Distance (kpc)	References[a]	Galactic/*IRAS* Name	Comments[b]
IRAS 00338+6312	00 36 47.5	+63 29 02	0.9	1, 6	G121.30+0.66	GBT run 1
Mol 3	00 44 57.6	+55 47 18	7.7	2	IRAS 00420+5530	GBT run 1
NGC 281	00 52 25.2	+56 33 53	3.5	1, 7	IRAS 00494+5617	GBT run 1
W3 IRS5	02 25 40.8	+62 05 53	2.3	8	G133.72+1.22	GBT run 1, five-point scan
IRAS 02395+6244	02 43 29.1	+62 56 59	9.1	1, 9	G135.28+2.80	GBT run 1
IRAS 02461+6147	02 50 09.2	+61 59 58	2.4	1, 10	G136.38+2.27	GBT run 1
IRAS 02541+6208	02 58 13.2	+62 20 29	2.4	1, 10	G137.07+3.00	GBT run 1
AFGL 490	03 27 38.8	+58 47 00	0.9	1, 10	IRAS 03236+5836	GBT run 1
Mol 7	05 01 39.7	+47 07 23	2.5	2	IRAS 04579+4703	GBT run 1
Mol 8	05 17 13.3	+39 22 14	10.8	2	IRAS 05137+3919	GBT run 1
IRAS 05358+3543	05 39 13.0	+35 45 49	1.8	3, 25	G173.48+2.43	GBT run 1
Mol 12	05 40 24.4	+23 50 54	1.2	2	IRAS 05373+2349	GBT run 1
G192.16−03.84	05 58 13.9	+16 32 00	2.0	11	IRAS 05553+1631	GBT run 1
S241	06 03 53.6	+30 14 44	5.3	1, 12	G180.87+4.09	GBT run 1
NGC 2264–IRS1	06 41 09.8	+09 29 32	0.8	13	G203.32+2.06	GBT run 1
Mol 28	07 00 51.0	−08 56 29	4.5	2	IRAS 06584−0852	GBT run 1
IRAS 07299−1651	07 32 09.8	−16 58 13	1.4	14	G232.62+1.00	GBT run 1
G5.63+0.24	17 57 33.3	−23 58 22	...	24	IRAS 17545−2357	GBT run 2
G5.89−0.39	18 00 30.9	−24 04 17	2.6	22, 26	IRAS 17574−2403	GBT run 2
G10.46+0.03	18 08 35.5	−19 52 09	10.9	18	IRAS 18056−1952	GBT run 2, three-point scan
G10.31−0.15	18 08 58.5	−20 05 24	15.0	18	IRAS 18060−2005	GBT run 2, three-point scan
G10.16−0.35	18 09 24.4	−20 19 29	14.6	18	IRAS 18064−2020	GBT run 2, three-point scan
G10.96+0.02	18 09 39.4	−19 26 27	14.0	18	IRAS 18067−1927	VLA, $V_{\rm LSR} = 20$ km s^{-1}, C1
G13.13−0.15	18 14 41.3	−17 37 04	12.4	18	IRAS 18117−1738	VLA, $V_{\rm LSR} = 40$ km s^{-1}, C1
IRAS 18151−1208	18 17 57.1	−12 07 22	3.0	2, 3	G18.34+1.77	GBT run 2
G14.68−0.50	18 19 04.2	−16 25 14	13.4	18	IRAS 18161−1626	GBT run 2, three-point scan
G19.36−0.02	18 26 24.3	−12 03 47	12.0	18	IRAS 18236−1205	GBT run 2, three-point scan
G19.07−0.28	18 26 47.0	−12 26 32	4.7	18	IRAS 18239−1228	VLA, $V_{\rm LSR} = 60$ km s^{-1}, C2
G19.62−0.23	18 27 38.0	−11 56 35	4.5	22	IRAS 18248−1158	GBT run 2
G20.08−0.14	18 28 10.4	−11 28 49	4.1	22	IRAS 18253−1130	GBT run 2
G23.43−0.21	18 34 43.6	−08 32 25	6.0	18	IRAS 18319−0834	VLA, $V_{\rm LSR} = 100$ km s^{-1}, C2
G23.71−0.20	18 35 12.5	−08 17 47	10.6	18	IRAS 18324−0820	VLA, $V_{\rm LSR} = 80$ km s^{-1}, C2
G24.50−0.06	18 36 11.0	−07 31 12	6.4	18	IRAS 18334−0733	GBT run 2, five-point scan
G24.51−0.22	18 36 46.8	−07 35 41	...	18	IRAS 18340−0738	GBT run 2, three-point scan
G24.68−0.16	18 36 51.8	−07 24 48	...	18	IRAS 18341−0727	VLA, $V_{\rm LSR} = 60$ km s^{-1}, C2
G28.20−0.05	18 42 58.2	−04 14 05	9.1	18, 23	IRAS 18403−0417	GBT run 2, three-point scan
G28.61+0.02	18 43 28.5	−03 50 19	...	18	IRAS 18408−0353	VLA, $V_{\rm LSR} = 90$ km s^{-1}, C2
G28.86+0.06	18 43 46.3	−03 35 29	7.4	18	IRAS 18411−0338	GBT run 2, three-point scan
G30.84−0.11	18 48 01.3	−01 54 49	...	18	IRAS 18454−0158	VLA, $V_{\rm LSR} = 90$ km s^{-1}, C2
IRAS 18470−0044	18 49 36.7	−00 41 05	8.2	3	G32.11+0.09	GBT run 1
Mol 75	18 53 38.1	+01 50 27	3.9	2, 19	IRAS 18511+0146	GBT run 2, three-point scan
IRAS 18521+0134	18 54 40.8	+01 38 02	...	19	G34.76+0.02	GBT run 2, three-point scan
IRAS 18566+0408	18 59 10.0	+04 12 16	6.7	4	G37.55+0.20	GBT runs 1 and 2
IRAS 19035+0641	19 06 01.1	+06 46 35	2.4	21	G40.62−0.14	GBT run 2
IRAS 19095+0930	19 11 53.3	+09 35 46	3.2	21	G43.79−0.13	GBT run 2
G43.18−0.52	19 12 10.2	+08 52 14	6.2	20	IRAS 19097+0847	VLA, $V_{\rm LSR} = 60$ km s^{-1}, C3
G49.21−0.35	19 23 02.5	+14 16 41	5.6	18	IRAS 19207+1410	VLA, $V_{\rm LSR} = 60$ km s^{-1}, C3
IRDC 1923+13	19 23 02.7	+13 58 00	...	19	G48.93−0.50	GBT run 2, three-point scan
IRAS 20126+4104	20 14 26.0	+41 13 32	1.7	15	G78.12+3.64	GBT run 1
MWC 349	20 32 45.5	+40 39 37	1.2	16	IRAS 20310+4029	GBT run 1
Mol 136	21 32 31.5	+51 02 22	4.9	2	IRAS 21307+5049	GBT run 1
Mol 138	21 40 42.4	+58 16 10	0.8	2	IRAS 21391+5802	GBT run 1
Mol 145[c]	22 21 22.5	+63 51 13	1.3	2	IRAS 22198+6336	GBT run 1, five-point scan

TABLE 1—*Continued*

Source	α(2000.0)	δ(2000.0)	Distance (kpc)	References[a]	Galactic/*IRAS* Name	Comments[b]
Mol 148	22 32 24.3	+58 18 58	5.4	2	IRAS 22305+5803	GBT runs 1 and 2
NGC 7538	23 13 45.4	+61 28 10	3.0	5	G111.54+0.78	GBT run 1
S157	23 16 04.4	+60 01 41	3.5	1, 17	G111.28−0.67	GBT run 1
IRAS 23139+5939	23 16 09.3	+59 55 23	4.8	3	G111.25−0.77	GBT runs 1 and 2
Mol 160	23 40 53.3	+61 10 19	6.9	2	IRAS 23385+6053	GBT run 1

NOTE.—Units of right ascension are hours, minutes, and seconds, and units of declination are degrees, arcminutes, and arcseconds.

[a] References for position and distance.

[b] *GBT observations.*—We list the observation date (run 1: 2004 October; run 2: 2005 July) and whether a five- or three-point scan was obtained. The H_2CO spectra of the central pointing position of the three-point scans were previously obtained by our group (Araya et al. 2004b; Sewiło et al. 2004) and were not reobserved as part of this work. *VLA observations.*—We list the central bandpass velocity and the secondary (phase) calibrator (C1: J1820−254, C2: J1832−105, C3: J1922+155).

[c] LDN 1204 A dark nebula; SIMBAD (http://simbad.u-strasbr.fr).

REFERENCES.—(1) Palagi et al. 1993; (2) Molinari et al. 1996; (3) Sridharan et al. 2002; (4) Araya et al. 2005b; (5) Hoffman et al. 2003; (6) Fiebig et al. 1996; (7) Henning et al. 1994; (8) Claussen et al. 1994; (9) Rudolph et al. 1996; (10) Lada & Lada 2003; (11) Shepherd et al. 2004; (12) Vallée 1987; (13) Schreyer et al. 1997; (14) Henning et al. 1992; (15) Cesaroni et al. 1997; (16) Tafoya et al. 2004; (17) Israel 1980; (18) Sewiło et al. 2004 or based on Sewiło et al. 2004 data; (19) Araya et al. 2004b; (20) tentative distance based on Watson et al. 2003 data; (21) Araya et al. 2005a; (22) Wood & Churchwell 1989; (23) Kurtz et al. 1994; (24) Codella et al. 1995; (25) Beuther et al. 2002; (26) Kim & Koo 2001.

absorption that could mask emission lines. However, in this survey we also extended our selection criteria to include (1) (radio-) bright star-forming regions to look for strong ($\sim$1 Jy) masers (in this group we included sources that have been observed before in the H_2CO 6 cm line to look for maser flares; e.g., see Mehringer et al. 1995) and (2) sources whose H_2CO 6 cm single-dish spectra from Paper I or Sewiło et al. (2004) were consistent with H_2CO 6 cm emission blended with absorption and that were not observed with the VLA in this work (see § 2.2). For the sources in group 2, we obtained H_2CO spectra at two positions, one telescope beam north and south from the positions observed in Paper I and Sewiło et al. (2004), to check whether the complex absorption profiles were extended (which would indicate that the asymmetries in the absorption lines are not due to H_2CO maser emission) or localized (which would be consistent with H_2CO maser emission at the central position). In addition, we obtained five-point cross scans toward three of the sources in our sample (W3 IRS5, G24.50−0.06, and Mol 145).

We also observed the H_2CO 6 cm maser sources IRAS 18566+0408 (Araya et al. 2005b) and NGC 7538 (e.g., Hoffman et al. 2003) to monitor the variability of the formaldehyde emission in the regions. In addition, we included the source MWC 349, which possibly is a young B[e] star that shows ionized gas distributed perpendicular to a dust disk (e.g., Danchi et al. 2001).

The observations were conducted in two epochs, 2004 October and 2005 July, with the GBT C-band receiver located at the Gregorian focus. We observed the $J_{KaKc} = 1_{11}$–1_{10} transition of formaldehyde ($\nu_0 = 4829.6594$ MHz,[9] H_2CO 6 cm line) and the radio recombination line H110α ($\nu_0 = 4874.157$ MHz) simultaneously, with a bandwidth per subcorrelator of 12.5 MHz ($\sim$770 km s^{-1}) and 16,384 channels (initial channel width of 0.76 kHz, 0.05 km s^{-1}). Both linear polarization signals were recorded. The lines He110α ($\nu_0 = 4876.143$ MHz) and C110α ($\nu_0 = 4876.589$ MHz)[10] were also observed simultaneously given that their rest frequencies are within the 12.5 MHz bandpass of the H110α subcorrelator. The goal of observing the hydrogen, helium, and carbon recombination lines (HRRLs, HeRRLs, and CRRLs, respectively) was to simultaneously obtain the LSR velocity of the ionized and photodissociation regions to compare with the LSR velocity of any new H_2CO maser detected.

The observation procedure was ON-OFF[11] with 5 minutes spent on both ON and OFF (reference) positions per scan. The reference position was chosen to match the azimuth-elevation path tracked by the telescope during the corresponding 5 minute ON-source observation. The system temperature was $\sim$24 K in the 2004 October run and $\sim$28 K during the 2005 July run. Periodically (approximately 3 times per night), we observed 3C 48, 3C 147, and NGC 7027 (in the 2004 October run) and 3C 48 and 3C 286 (in the 2005 July run) in continuum mode to obtain pointing corrections and to measure the telescope beamwidth. We derived focus corrections from 3C 48 and 3C 147 observations in the 2004 October run and from 3C 48 and 3C 286 in the 2005 July run. The pointing corrections were always smaller than 0.6′; we measured a telescope beamwidth of 2.5′. After pointing and focus corrections were applied, the calibrator sources were observed in the same spectral line mode as the program sources to determine the telescope gain (see below).

We obtained the antenna temperature spectra using the routine `d.calib` in AIPS++.[12] The scans were inspected to check for consistency and RFI, and to flag corrupted data. We also inspected the OFF-source spectra to check for line contamination at the reference position that could mimic emission features. Then the spectra were exported to CLASS[13] for subsequent calibration and analysis.

The 2004 October data were calibrated using a gain of 1.90 K Jy^{-1}, which was obtained from observations of 3C 48, 3C 147, and NGC 7027, assuming a flux density of $S_\nu = 5.47$ Jy for 3C 48, $S_\nu = 7.94$ Jy for 3C 147, and $S_\nu = 5.37$ Jy for NGC 7027. The 1 σ dispersion of the telescope gain measurements derived from the 3C 48, 3C 147, and NGC 7027 observations is $\sim$6% of the average gain value. We calibrated the 2005 July spectra using a telescope gain value of 1.95 K Jy^{-1} obtained from observations of 3C 48 and 3C 286. Based on the telescope gain dispersion obtained from the 3C 48 and 3C 286 measurements, we estimate a 1 σ confidence level of $\sim$7% in the calibration of the

[9] This value is the weighted average frequency of the $F = 2$−2 and $F = 0$−1 hyperfine components given in Tucker et al. (1970).

[10] The radio recombination line rest frequencies are from Gordon & Sorochenko (2002).

[11] A noise-diode signal was injected into the system every 1 s for antenna temperature calibration.

[12] AIPS++ is a software package of the National Radio Astronomy Observatory (NRAO).

[13] CLASS is part of the GILDAS software package developed by the Institut de Radio Astronomie Millimétrique (IRAM).

TABLE 2

H_2CO 6 cm Line Parameters from GBT Observations

Source	S_{H_2CO} (mJy)	V_{LSR} (km s^{-1})	Width (km s^{-1})	$\int S_\nu\, dv$ (mJy km s^{-1})	Notes[a]
IRAS 00338+6312.....	−446(5)	−17.37(0.01)	2.44(0.02)	−1158(9)	1
Mol 3.....	−72(4)	−51.19(0.03)	2.17(0.08)	−167(5)	1, A, H
NGC 281.....	−104(6)	−30.8(0.1)	4.0(0.1)	−446(11)	1
W3 IRS5	−4440(68)	−40.3(0.1)	11.1(0.1)	−15273(755)	2, M, V, W
	−831(68)	−21.0(0.1)	2.7(0.1)	−855(183)	2, M, V
W3 IRS5 N.....	−720(26)	−40.2(0.1)	9.7(0.1)	−2496(252)	2, A, V, W
	−107(26)	−21.2(0.1)	0.87(0.1)	−98(9)	2, A
W3 IRS5 S.....	−449(26)	−38.6(0.1)	6.3(0.1)	−1200(164)	2, A, V
	−107(26)	−21.5(0.1)	1.95(0.1)	−223(13)	2, A
W3 IRS5 E	−489(23)	−40.2(0.1)	7.0(0.1)	−1534(161)	2, A, V
	−99(23)	−21.06(0.03)	0.60(0.08)	−63(6)	2, A
W3 IRS5 W	−904(27)	−39.7(0.1)	17.2(0.1)	−5499(464)	2, M, V, W
IRAS 02395+6244.....	(5)	...	...	...	1, N
IRAS 02461+6147.....	(5)	...	...	...	1, N
IRAS 02541+6208.....	−30(5)	−51.9(0.1)	2.1(0.3)	−68(8)	1
AFGL 490.....	−237(4)	−12.75(0.01)	2.84(0.03)	−719(6)	1, A
Mol 7.....	−51(3)	−17.4(0.4)	5.7(0.8)	−139(18)	1, V
	−24(3)	−6.8(0.1)	1.7(0.2)	−43(3)	1, A, H
Mol 8.....	−41(3)	−25.45(0.06)	2.3(0.2)	−102(5)	1
IRAS 05358+3543.....	−228(5)	−16.96(0.02)	3.92(0.05)	−953(10)	1, A
Mol 12.....	−347(4)	2.40(0.01)	2.52(0.02)	−929(6)	1
G192.16−03.82.....	−32(2)	5.75(0.09)	2.8(0.2)	−95(6)	1, O, M
S241	−88(5)	−7.36(0.06)	4.3(0.1)	−406(11)	1, A
NGC 2264–IRS1	−401(5)	6.8(0.4)	16.5(0.8)	−1928(87)	1, V, W
Mol 28.....	−97(3)	40.49(0.02)	2.12(0.05)	−218(4)	1, O
IRAS 07299−1651	−93(5)	16.89(0.04)	2.4(0.1)	−240(7)	1
G5.63+0.23	−293(4)	8.7(0.4)	21.3(0.8)	−1942(85)	1, V, W
G5.89−0.39.....	−236(6)	18.94(0.02)	5.15(0.06)	−1296(13)	1, 3G
	−227(6)	10.19(0.03)	4.25(0.07)	−1029(25)	1, 3G
	−102(6)	1.6(0.1)	10.9(0.4)	−1182(33)	1, 3G
G10.46+0.03 N.....	−128(7)	66.70(0.09)	5.6(0.2)	−754(24)	3, A
	−31(7)	154.7(0.2)	2.5(0.5)	−84(16)	3, A
	−19(7)	24.4(0.4)	4.6(0.7)	−91(15)	3, A
	−19(6)	6.5(0.4)	3.8(0.7)	−75(14)	3, A
G10.46+0.03	−238(10)	68.9(0.1)	8.3(0.1)	−2110(30)	3
	−124(10)	25.8(0.1)	2.3(0.2)	−310(20)	3
	−29(9)	155.5(0.3)	3.5(0.6)	−110(20)	3
	−34(6)	9.4(0.2)	2.3(0.7)	−80(20)	3, 2G
	−29(6)	7.4(0.2)	1.3(0.3)	−40(20)	3, 2G
	−68(7)	34.6(0.1)	1.8(0.2)	−130(10)	3, 4G
	−44(7)	30.1(0.1)	1.0(0.2)	−47(6)	3, 4G
	−40(7)	32.0(0.1)	1.5(0.3)	−60(10)	3, 4G
	−32(7)	33.0(0.1)	0.4(0.1)	−13(5)	3, 4G
G10.46+0.03 S.....	−113(7)	68.5(0.1)	8.5(0.4)	−1028(35)	3, A
	−40(7)	25.8(0.3)	3.3(0.6)	−140(22)	3
	−39(7)	−10.4(0.3)	4.5(0.7)	−187(25)	3
	−27(7)	33.7(0.5)	4.1(1.1)	−116(24)	3
G10.31−0.15 N.....	−251(8)	11.09(0.04)	4.1(0.1)	−1101(21)	3
	−120(8)	23.4(0.1)	6.8(0.3)	−871(33)	3, 2G
	−51(8)	28.9(0.1)	2.0(0.3)	−112(20)	3, 2G
	−95(8)	39.6(0.1)	3.5(0.3)	−351(30)	3, 2G
	−93(8)	44.5(0.2)	4.3(0.3)	−422(32)	3, 2G
G10.31−0.15.....	−480(40)	11.1(0.1)	5.3(0.1)	−2700(30)	3, 2G
	−120(40)	3.9(0.1)	4.1(0.2)	−520(30)	3, 2G
	−298(23)	22.3(0.1)	6.2(0.3)	−1980(80)	3, 2G
	−130(23)	28.3(0.2)	3.5(0.4)	−480(60)	3, 2G
	−428(49)	38.4(0.1)	1.8(0.1)	−820(40)	3
	−50(15)	47.3(0.4)	7.8(0.8)	−420(40)	3
G10.31−0.15 S.....	−209(6)	12.41(0.04)	4.4(0.2)	−974(42)	3, 4G
	−37(6)	5.5(0.4)	5.2(0.9)	−204(34)	3, 4G
	−73(6)	20.1(0.2)	4.1(0.8)	−316(26)	3, 4G
	−69(6)	27.0(0.2)	4.5(0.4)	−327(36)	3, 4G
	−114(6)	38.07(0.08)	3.1(0.2)	−369(20)	3

TABLE 2—*Continued*

Source	S_{H_2CO} (mJy)	V_{LSR} (km s^{-1})	Width (km s^{-1})	$\int S_\nu\, dv$ (mJy km s^{-1})	Notes[a]
G10.16−0.35 N	−2280(14)	11.80(0.08)	6.7(0.2)	−16213(461)	1, 2G
	−466(14)	2.9(0.5)	8.0(1.0)	−3970(474)	1, 2G
	−334(14)	25.87(0.08)	1.9(0.2)	−683(65)	1, 3G
	−214(14)	30.8(0.2)	3.1(0.4)	−716(74)	1, 3G
	−130(14)	28.0(0.2)	1.5(0.5)	−204(78)	1, 3G
	−149(14)	36.7(0.2)	3.3(0.4)	−529(56)	1, A
G10.16−0.35	−765(97)	36.2(0.1)	1.8(0.2)	−1460(100)	1
	−658(97)	26.5(0.1)	3.8(0.3)	−2660(150)	1
	−641(97)	31.4(0.1)	2.2(0.2)	−1490(120)	1
	−2623(190)	9.0(0.3)	7.1(0.6)	−19860(1960)	1, 3G
	−2262(190)	1.1(0.2)	6.4(0.4)	−15450(1170)	1, 3G
	−1406(190)	16.2(0.4)	6.8(0.7)	−10240(1500)	1, 3G
G10.16−0.35 S	−334(10)	9.7(0.2)	5.2(0.7)	−1826(320)	1, 3G
	−237(10)	16.0(0.4)	5.6(0.8)	−1403(226)	1, 3G
	−127(10)	1.3(0.7)	9.1(1.6)	−1223(202)	1, 3G
	−152(10)	26.55(0.07)	2.4(0.2)	−387(23)	1, 2G
	−39(10)	30.9(0.3)	3.4(0.5)	−142(5)	1, 2G
	−63(10)	36.3(0.2)	2.1(0.4)	−139(22)	1
IRAS 18151−1208	−75(4)	32.26(0.05)	3.3(0.1)	−237(7)	1, O
G14.68−0.50 N	−125(5)	27.76(0.05)	3.6(0.1)	−478(15)	3
	−30(5)	60.4(0.2)	1.6(0.3)	−51(10)	3
	−20(5)	18.9(0.4)	3.2(0.9)	−67(15)	3
G14.68−0.50	−97(4)	27.7(0.1)	4.0(0.1)	−420(10)	3
	−45(4)	19.3(0.1)	4.0(0.3)	−190(10)	3
	−25(4)	38.0(0.1)	1.7(0.3)	−50(10)	3
	−21(4)	60.0(0.1)	1.3(0.3)	−30(10)	3
	−21(4)	44.5(0.1)	0.7(0.3)	−20(10)	3
	−13(4)	71.7(0.2)	1.1(0.5)	−20(10)	3
G14.68−0.50 S	−90(6)	18.41(0.09)	3.9(0.2)	−372(18)	3
	−55(6)	28.8(0.1)	2.9(0.4)	−171(18)	3, 2G
	−34(6)	25.4(0.2)	1.9(0.4)	−69(14)	3, 2G
	−28(6)	60.1(0.2)	1.4(0.4)	−43(11)	3
G19.36−0.02 N	−317(9)	26.67(0.02)	3.41(0.06)	−1150(16)	1, A
	−35(9)	−24.38(0.07)	0.6(0.3)	−21(6)	1
	−28(9)	68.0(0.3)	4.2(0.7)	−124(17)	1
G19.36−0.02	−380(6)	26.9(0.1)	3.2(0.1)	−1300(10)	1, 2G
	−67(6)	23.1(0.1)	1.8(0.2)	−130(10)	1, 2G
	−32(5)	67.9(0.2)	2.9(0.5)	−100(10)	1
	−19(5)	39.6(0.2)	3.2(0.6)	−70(10)	1
	−19(5)	71.6(0.3)	1.6(0.8)	−30(10)	1, 3G
	−24(3)	117.0(0.1)	1.8(0.4)	−50(10)	1, 3G
	−12(3)	120.6(0.5)	4.5(1.0)	−60(10)	1, 3G
G19.36−0.02 S	−209(10)	26.45(0.03)	2.28(0.07)	−506(14)	1, A
G19.62−0.23	−1043(8)	44.62(0.01)	6.18(0.03)	−6854(27)	1, 2G
	−267(8)	51.73(0.03)	2.80(0.09)	−796(21)	1, 2G
	−96(8)	71.7(0.1)	4.3(0.4)	−443(33)	1, 2G
	−46(8)	64.89(0.08)	4.2(0.8)	−207(34)	1, 2G
	−82(8)	99.9(0.1)	3.0(0.2)	−263(18)	1, A
	−42(8)	119.2(0.2)	2.4(0.5)	−110(16)	1, A
	−31(8)	6.9(0.1)	0.9(0.3)	−29(6)	1
G20.08−0.14	−419(4)	43.26(0.01)	4.77(0.03)	−2127(12)	1
	−284(4)	57.15(0.02)	2.95(0.04)	−891(13)	1, 2G
	−50(4)	61.53(0.06)	4.1(0.4)	−220(16)	1, 2G, M
	−40(4)	119.00(0.06)	1.8(0.1)	−75(5)	1
	−18(4)	6.54(0.08)	1.2(0.2)	−23.6(3)	1
G24.50−0.06	−249(7)	48.78(0.03)	2.94(0.07)	−778(16)	3, 3G
	−56(7)	44.1(0.1)	2.6(0.3)	−154(14)	3, 3G
	−46(7)	53.3(0.2)	2.6(0.4)	−127(15)	3, 3G
	−157(7)	110.36(0.08)	4.8(0.2)	−806(29)	3, W
	−74(7)	5.7(0.1)	2.7(0.3)	−211(16)	3, A
	−65(7)	83.7(0.1)	2.5(0.3)	−169(16)	3
G24.50−0.06 N	−130(6)	49.29(0.07)	3.6(0.2)	−490(20)	3, 2G
	−39(6)	44.5(0.2)	3.2(0.4)	−135(17)	3, 2G

TABLE 2—*Continued*

Source	S_{H_2CO} (mJy)	V_{LSR} (km s^{-1})	Width (km s^{-1})	$\int S_\nu\, dv$ (mJy km s^{-1})	Notes[a]
G24.50−0.06 S	−89(6)	48.6(0.2)	4.2(0.5)	−398(36)	3, 2G, W
	−59(6)	44.1(0.2)	3.2(0.4)	−199(32)	3, 2G
	−64(6)	5.54(0.09)	1.8(0.3)	−123(15)	3
	−44(6)	109.3(0.3)	6.7(0.7)	−315(26)	3
	−31(6)	84.8(0.2)	2.0(0.6)	−65(15)	3
G24.50−0.06 E	−137(7)	43.99(0.08)	2.7(0.2)	−393(22)	3, 2G
	−136(7)	49.24(0.08)	2.9(0.2)	−426(24)	3, 2G
	−54(7)	95.1(0.2)	3.4(0.4)	−195(20)	3
	−22(7)	7.3(0.3)	3.1(0.6)	−71(13)	3 A
G24.50−0.06 W	−186(7)	109.74(0.07)	5.9(0.2)	−1169(29)	3, A, W
	−178(7)	48.97(0.06)	2.8(0.2)	−530(29)	3, 2G, W
	−88(7)	45.4(0.1)	2.3(0.3)	−210(24)	3, 2G
	−65(7)	5.7(0.1)	2.3(0.3)	−162(15)	3
	−40(7)	87.8(0.2)	2.5(0.6)	−108(21)	3, A
G24.51−0.22 N	−81(6)	100.1(0.1)	3.8(0.3)	−332(20)	3, A
	−78(6)	45.7(0.1)	3.7(0.3)	−310(21)	3, 2G
	−71(6)	41.7(0.1)	2.7(0.2)	−201(18)	3, 2G
	−46(6)	51.9(0.2)	1.9(0.4)	−91(32)	3, 2G
	−46(6)	54.4(0.3)	2.6(0.9)	−128(38)	3, 2G
	−24(6)	7.3(0.1)	1.6(0.3)	−41(6)	3
G24.51−0.22	−156(12)	45.2(0.1)	3.7(0.2)	−610(30)	3, 3G
	−117(12)	41.5(0.1)	2.1(0.1)	−260(10)	3, 3G
	−47(12)	43.3(0.1)	0.7(0.2)	−40(20)	3, 3G
	−62(5)	54.8(0.1)	2.1(0.3)	−140(20)	3, 2G
	−58(5)	52.6(0.1)	1.7(0.2)	−100(30)	3, 2G
	−48(9)	99.9(0.2)	4.8(0.5)	−250(20)	3
G24.51−0.22 S	−130(7)	44.81(0.07)	4.1(0.2)	−568(18)	3, A
	−96(7)	57.9(0.2)	5.6(0.4)	−578(34)	3, 2G
	−52(7)	53.9(0.1)	2.1(0.3)	−114(25)	3, 2G
	−30(7)	96.8(0.3)	2.3(0.7)	−71(21)	3, 2G
	−26(7)	99.8(0.4)	2.5(1.0)	−67(24)	3, 2G
G28.20−0.05 N	−88(9)	96.4(0.2)	2.1(0.5)	−194(26)	1, 2G
	−40(9)	96.4(0.9)	7.9(2.4)	−331(86)	1, 2G
	−87(9)	76.5(0.2)	4.3(0.4)	−397(40)	1, 2G
	−31(9)	81.2(0.5)	3.4(1.2)	−111(40)	1, 2G
	−26(9)	108.3(0.3)	2.5(0.6)	−69(15)	1, A
G28.20−0.05	−351(16)	97.1(0.1)	4.4(0.1)	−1640(30)	1, 2G
	−118(16)	90.9(0.1)	4.6(0.3)	−560(30)	1, 2G
	−207(16)	77.8(0.1)	4.1(0.1)	−910(20)	1
	−80(13)	105.8(0.1)	3.2(0.4)	−270(20)	1
	−21(6)	45.8(0.3)	6.3(1.0)	−140(20)	1
G28.20−0.05 S	−96(9)	97.38(0.09)	3.0(0.2)	−306(36)	1, 3G
	−38(9)	103.6(0.4)	7.5(1.8)	−304(58)	1, 3G
	−24(9)	110.4(0.4)	3.0(0.7)	−76(25)	1, 3G
	−76(9)	77.3(0.1)	3.2(0.2)	−260(16)	1, M
G28.86+0.06 N	−124(9)	81.60(0.06)	2.7(0.1)	−356(15)	1, A
	−60(9)	94.4(0.2)	2.8(0.4)	−178(19)	1, 2G
	−66(9)	98.7(0.1)	3.0(0.3)	−212(20)	1, 2G
	−59(9)	52.7(0.1)	2.8(0.3)	−173(16)	1
	−30(9)	69.8(0.2)	2.1(0.4)	−65(13)	1, A
G28.86+0.06	−305(14)	100.3(0.1)	3.6(0.1)	−1180(20)	1
	−169(5)	80.5(0.1)	3.0(0.1)	−550(10)	1
	−95(10)	52.4(0.1)	2.6(0.2)	−260(20)	1
	−50(14)	94.2(0.1)	2.3(0.3)	−120(10)	1
	−24(5)	72.0(0.1)	2.2(0.3)	−60(10)	1
G28.86+0.06 S	−224(9)	100.29(0.03)	3.20(0.08)	−762(16)	1, A
	−103(9)	80.30(0.07)	2.9(0.2)	−317(15)	1, A
	−90(9)	49.0(0.1)	4.2(0.2)	−401(18)	1, A
IRAS 18470−0044	−121(3)	95.94(0.02)	3.13(0.05)	−403(5)	1, A, W
	−19(3)	9.17(0.08)	1.7(0.2)	−35(3)	1
Mol 75 N	−133(6)	57.55(0.07)	2.7(0.2)	−386(28)	3, 2G
	−100(6)	53.6(0.1)	4.1(0.3)	−439(30)	3, 2G
	−25(6)	90.2(0.2)	3.6(0.6)	−99(14)	3, A
	−22(6)	80.5(0.2)	0.9(0.3)	−21(7)	3
Mol 75	−75(1)	58.0(0.8)	18.9(1.5)	−356(17)	3, M, V

TABLE 2—*Continued*

Source	S_{H_2CO} (mJy)	V_{LSR} (km s^{-1})	Width (km s^{-1})	$\int S_\nu\, dv$ (mJy km s^{-1})	Notes[a]
Mol 75 S	−200(7)	58.42(0.05)	2.1(0.1)	−456(20)	3
	−154(7)	53.14(0.07)	2.6(0.2)	−420(23)	3, 2G
	−68(7)	49.5(0.1)	1.6(0.3)	−117(19)	3, 2G
IRAS 18521+0134 N	−39(5)	27.9(0.3)	2.0(0.5)	−81(21)	3, O
	−29(5)	48.5(0.6)	3.8(1.5)	−115(36)	3, 2G
	−26(5)	44.2(0.6)	2.7(1.1)	−74(32)	3, 2G
	−25(5)	78.6(0.2)	1.6(0.4)	−42(9)	3
IRAS 18521+0134	−10(1)	28.4(0.3)	2.0(0.5)	−22.1(6)	3, O
	−37(1)	43.3(0.8)	12.9(1.5)	−160(14)	3, V
	−43(1)	77.0(0.8)	12.9(1.5)	−198(14)	3, V
	−16(1)	90.5(0.4)	1.9(1.2)	−33(9)	3
IRAS 18521+0134 S	−158(5)	90.53(0.04)	2.4(0.1)	−406(15)	3
	−81(5)	78.1(0.8)	19.7(1.5)	−587(95)	3, M, V
	−66(5)	43.4(0.1)	3.5(0.3)	−249(16)	3
	−27(5)	36.1(0.2)	2.1(0.5)	−62(12)	3, O
IRAS 18566+0408	−299(3)	85.46(0.01)	4.63(0.04)	−1473(9)	1, A, W
	−30(3)	18.7(0.1)	1.6(0.2)	−52(7)	1
	−29(3)	21.22(0.09)	1.1(0.3)	−36(6)	1
	−15(3)	5.3(0.4)	3.8(0.8)	−29(12)	1, V
	−11(3)	11.4(0.4)	2.6(0.8)	−21(7)	1, V
Maser	24(3)	79.8(0.1)	1.0(0.3)	26(4)	1
IRAS 19035+0641	−106(4)	32.95(0.05)	5.3(0.1)	−593(12)	1, A, O
	−28(4)	19.2(0.1)	2.2(0.3)	−64(7)	1
	−11(4)	43.7(0.4)	2.2(0.6)	−26(8)	1 T
IRAS 19095+0930	−57(4)	42.6(0.2)	3.5(0.3)	−212(19)	1, 2G
	−28(4)	46.1(0.3)	2.9(0.5)	−88(19)	1, 2G
	−36(4)	59.9(0.4)	6.1(0.8)	−89(24)	1, V, H
IRDC 1923+13 N	−173(7)	57.72(0.05)	2.6(0.1)	−478(18)	3
IRDC 1923+13	−4(1)	6.7(0.1)	1.0(0.7)	−4.3(1.2)	3
	−12(1)	50.2(0.8)	6.1(1.5)	−32.2(4.9)	3, V
	−9(1)	57.56(0.09)	2.6(0.2)	−25.2(1.7)	3
IRDC 1923+13 S	−31(8)	56.8(0.8)	12.9(1.5)	−194(101)	3, V
IRAS 20126+4104	−23(5)	−3.7(0.3)	3.3(0.6)	−83(14)	1, O
MWC 349	(3)	...	...	...	1, N
Mol 136	−12(3)	−46.9(0.2)	3.1(0.6)	−40(6)	1
Mol 138	−104(2)	0.68(0.02)	2.90(0.04)	−321(4)	1, A
Mol 145	−130(2)	−11.27(0.02)	2.00(0.04)	−278(8)	1, 2G
	−45(2)	−8.61(0.08)	2.6(0.2)	−126(8)	1, 2G
Mol 145 N	−124(10)	−10.73(0.07)	2.0(0.2)	−259(20)	1, 2G
	−52(10)	−8.6(0.1)	1.3(0.4)	−73(19)	1, 2G
	−42(10)	−2.78(0.07)	0.5(0.2)	−22(4)	1
Mol 145 S	−88(8)	−11.22(0.05)	1.7(0.2)	−158(11)	1
	−40(8)	−7.7(0.1)	1.6(0.4)	−66(11)	1
Mol 145 E	−33(8)	−11.1(0.1)	2.2(0.4)	−77(12)	1
	−23(8)	−7.1(0.2)	1.9(0.6)	−47(11)	1
Mol 145 W	−97(8)	−11.34(0.04)	2.1(0.1)	−215(9)	1, 2G
	−36(8)	−8.61(0.08)	0.9(0.2)	−36(7)	1, 2G
Mol 148	−72(2)	−52.73(0.01)	2.48(0.03)	−189(2)	1, O
NGC 7538	−218(14)	−55.95(0.05)	6.7(0.1)	−1544(27)	2, 3G, M
Maser	444(14)	−60.12(0.01)	0.84(0.02)	398(9)	2, 3G
	1310(14)	−57.91(0.01)	0.94(0.01)	1315(10)	2, 3G
S157	−64(4)	−43.09(0.05)	3.4(0.1)	−226(8)	1
IRAS 23139+5939	−31(2)	−44.02(0.05)	2.66(0.11)	−88(3)	1
Mol 160	−117(3)	−47.7(0.4)	11.0(0.8)	−372(35)	1, V, W

NOTES.—Spectrum rms is reported as S_{H_2CO} error. Other uncertainties shown in parentheses are 1 σ statistical errors from the fit. The line parameters of the central position of the three-point scans were obtained by Sewiło et al. (2004) or Araya et al. (2004b) and are reported here for completeness. In the case of the Sewiło et al. (2004) data, instead of the rms we list the reported error in the flux density measurement. (1) Spectrum smoothed to a channel width of 6.1 kHz (0.38 km s^{-1}). (2) Spectrum smoothed to a channel width of 0.76 kHz (0.05 km s^{-1}). (3) Spectrum smoothed to a channel width of 12.2 kHz (0.76 km s^{-1}). (O) H_2CO absorption at reference position. (V) Zero power full width (ZPFW) of an asymmetric or multiple peak line is presented. The flux density and V_{LSR} values are from the channel with deepest absorption. The reported V_{LSR} and ZPFW errors are one channel width and 2 times the channel width, respectively. As upper limit of the $\int S_\nu\, dv$ error we report 1 $\sigma \times$ ZPFW in parentheses. (A) Asymmetric line fitted with a single Gaussian profile. (M) Multipeak line. (2G, 3G, 4G) Multipeak line fitted with two, three, or four Gaussian profiles, respectively. (N) No detection. (H) Hyperfine structure detected or possibly detected. (W) Red or blue wing. (T) Tentative detection.

[a] Unless indicated otherwise, the line parameters were obtained by Gaussian fits to the line profiles. We report the FWHM as line width.

TABLE 3

RRL Parameters from GBT Observations

Source	S_ν (mJy)	V_{LSR} (km s^{-1})	Width (km s^{-1})	$\int S_\nu\, dv$ (mJy km s^{-1})	Notes[a]
IRAS 00338+6312	(2)	...	...	...	1, N
Mol 3	(1)	...	...	...	1, N
NGC 281	32(2)	−26.8(0.7)	22.7(1.7)	778(48)	H110α, 1
W3 IRS5	1692(18)	−40.97(0.06)	29.5(0.2)	53154(225)	H110α, 1
	172(18)	−40.1(0.6)	27.8(1.8)	5085(160)	He110α, 1
	142(18)	−40.6(0.5)	10.5(1.4)	1581(111)	C110α, 1
W3 IRS5 N	338(6)	−41.1(0.1)	28.6(0.3)	10300(91)	H110α, 1
	33(6)	−39.6(1.0)	25.6(2.9)	898(79)	He110α, 1
	32(6)	−40.1(0.6)	7.8(2.0)	264(53)	C110α, 1
W3 IRS5 S	322(5)	−41.58(0.09)	25.6(0.2)	8791(64)	H110α, 1
	26(5)	−42.0(1.5)	29.6(7.0)	828(129)	He110α, 1
	18(5)	−43.3(1.6)	13.2(3.3)	255(80)	C110α, 1
W3 IRS5 E	195(5)	−41.6(0.2)	27.3(0.4)	5679(69)	H110α, 1, W
	21(5)	−41.7(1.2)	21.5(3.1)	472(54)	He110α, 1
	19(5)	−40.9(0.8)	7.6(1.9)	150(33)	C110α, 1
W3 IRS5 W	300(5)	−44.62(0.09)	28.5(0.2)	9092(54)	H110α, 1
	25(5)	−49.8(0.9)	12.2(2.4)	330(53)	He110α, 1
	46(5)	−42.4(0.4)	8.8(1.0)	431(41)	C110α, 1
IRAS 02395+6244	(2)	...	...	...	1, N
IRAS 02461+6147	(2)	...	...	...	1, N
IRAS 02541+6208	(2)	...	...	...	1, N
AFGL 490	(1)	...	...	...	1, N
Mol 7	(1)	...	...	...	1, N
Mol 8	(1)	...	...	...	1, N
IRAS 05358+3543	(2)	...	...	...	1, N
Mol 12	(1)	...	...	...	1, N
G192.16−03.82	(0.8)	...	...	...	1, N
S241	8(2)	−6.1(1.2)	12.8(3.4)	111(21)	H110α, 1
NGC 2264–IRS1	(2)	...	...	...	1, N
Mol 28	(1)	...	...	...	1, N
IRAS 07299−1651	6.3(1.8)	14.6(1.6)	15.6(3.8)	105(20)	H110α, 1
	5.0(1.8)	14.1(1.6)	12.8(3.9)	68(17)	C110α^*, 1
G5.63+0.23	...	...	...	...	1, O
G5.89−0.39	187(2)	9.49(0.09)	23.7(0.2)	4714(34)	H110α, 1
	10(2)	8.6(1.8)	17.8(3.5)	195(44)	He110α, 1
G10.46+0.03 N	14(3)	65.1(1.4)	23.4(2.6)	360(40)	H110α, 1, O, A
G10.46+0.03	81(6)	70.2(0.3)	21.9(0.7)	1890(50)	H110α, 3
G10.46+0.03 S	42(3)	72.3(0.4)	19.7(1.0)	876(37)	H110α, 1, A
G10.31−0.15 N	111(3)	12.6(0.2)	29.0(0.6)	3435(60)	H110α, 1
	13(3)	11.5(1.6)	22.7(3.3)	315(44)	He110α, 1
	13(3)	14.6(1.2)	12.5(3.1)	166(38)	C110α, 1
G10.31−0.15	469(11)	9.4(0.1)	32.0(0.2)	15960(70)	H110α, 3
	35(11)	7.5(1.0)	36.1(2.4)	1338(77)	He110α, 3
G10.31−0.15 S	119(4)	5.6(0.2)	28.3(0.6)	3577(59)	H110α, 1
	10(4)	5.6(2.2)	25.1(7.4)	279(58)	He110α, 1
	7(4)	13.1(1.6)	6.1(3.1)	46(29)	C110α, T, 1
G10.16−0.35 N	367(5)	14.3(0.1)	34.9(0.3)	13602(95)	H110α, 1, W
	14(5)	9.5(2.8)	42.0(5.4)	643(79)	He110α, 1, B
G10.16−0.35	1494(26)	12.5(0.1)	32.9(0.1)	52350(19)	H110α, 3, W
	79(18)	7.4(0.8)	36.2(2.1)	3046(142)	He110α, 3
G10.16−0.35 S	177(4)	10.7(0.2)	36.5(0.5)	6867(79)	H110α, 1, W
	13(4)	8.3(2.3)	35.5(6.1)	499(69)	He110α, 1
	10(4)	1.8(1.6)	12.6(4.0)	128(44)	C110α, T, 1
IRAS 18151−1208	33(3)	24.4(0.3)	26.4(0.6)	920(19)	H110α, 3
	10(3)	32.1(0.3)	2.8(1.0)	30(8)	C110α, 3
G14.68−0.50 N	11(3)	11.9(1.9)	14.0(4.3)	157(43)	H110α, 1, 2G
	12(3)	28.7(1.5)	10.9(2.9)	143(39)	H110α, 1, 2G
	5(3)	9.5(3.2)	16.6(6.9)	96(31)	C110α, T, 1
G14.68−0.50	21(3)	27.5(0.5)	23.5(1.3)	510(20)	H110α, 5
G14.68−0.50 S	14(3)	29.3(1.5)	27.2(3.2)	395(40)	H110α, 1, A
G19.36−0.02 N	$\lesssim$5(1)	...	...	...	H110α, T, 4
G19.36−0.02	10(1)	51.1(0.8)	21.9(1.9)	220(20)	H110α, 5, A
G19.36−0.02 S	$\lesssim$7(3)	...	...	...	H110α, T, 1

TABLE 3—*Continued*

Source	S_ν (mJy)	$V_{\rm LSR}$ (km s^{-1})	Width (km s^{-1})	$\int S_\nu\, dv$ (mJy km s^{-1})	Notes[a]
G19.62−0.23.....	264(3)	41.3(0.1)	31.2(0.3)	8745(39)	H110α, 1, W
	23(3)	44.3(0.6)	15.9(1.3)	386(36)	He110α, 1, 2G
	11(3)	49.2(1.5)	21.5(3.9)	248(40)	C110α, 1, 2G
G20.08−0.14.....	49(2)	42.3(0.2)	28.8(0.5)	1508(22)	H110α, 1
	4(2)	37.6(1.7)	16.4(4.0)	75(17)	He110α, 1
	4(2)	42.6(1.7)	7.9(3.6)	32(12)	C110α, 1
G24.50−0.06.....	71(3)	114.3(3.0)	99.3(6.0)	2284(318)	H110α, 1, V
G24.50−0.06 N	38(3)	114.2(3.0)	75.6(6.0)	1294(205)	H110α, 1, V, A, W
	6(3)	115.7(2.1)	13.6(3.2)	80(22)	He110α, T, 1
G24.50−0.06 S.....	19(3)	101.1(1.8)	43.1(3.3)	850(70)	H110α, 1, M, 2G
	17(3)	85.5(0.7)	8.1(1.7)	144(36)	H110α, 1, M, 2G
	10(3)	105.7(1.6)	4.6(2.1)	50(15)	C110α, T, 1
G24.50−0.06 E.....	32(3)	90.2(3.0)	71.7(6.0)	1264(209)	H110α, 1, V
G24.50−0.06 W	53(3)	117.6(3.0)	69.1(6.0)	1656(207)	H110α, 1, V, W
G24.51−0.22 N	77(4)	93.0(0.3)	20.3(0.6)	1670(43)	H110α, 1
	35(4)	41.6(0.6)	17.6(1.3)	652(40)	H110α, 1, A
G24.51−0.22.....	126(8)	96.4(0.2)	23.0(0.4)	3090(40)	H110α, 3, A
	31(8)	44.3(0.6)	18.6(1.3)	600(40)	H110α, 3, A
	13(6)	93.8(1.0)	10.5(2.2)	146(26)	He110α, T, 3
G24.51−0.22 S.....	70(3)	97.0(0.3)	20.6(0.8)	1543(46)	H110α, 1, W
	19(3)	46.5(1.0)	17.8(2.2)	362(40)	H110α, 1, A
	10(3)	95.7(1.1)	9.0(2.5)	92(22)	He110α, T, 1
G28.20−0.05 N	16(3)	77.0(0.9)	12.7(2.0)	215(32)	H110α, 1, 2G
	14(3)	98.6(1.2)	16.6(3.1)	242(35)	H110α, 1, 2G
G28.20−0.05.....	32(5)	100.3(0.7)	22.1(1.7)	750(50)	H110α, 5, 2G
	13(5)	77.0(1.3)	14.6(3.1)	200(50)	H110α, 5, 2G
G28.20−0.05 S.....	15(3)	93.8(1.5)	40.9(3.4)	669(49)	H110α, 1, A
	6(3)	−103.2(4.5)	48.3(10.6)	294(55)	H110α, 1
G28.86+0.06 N	17(3)	102.2(3.0)	27.0(6.0)	264(86)	H110α, 1, A, V
G28.86+0.06	31(5)	101.7(0.4)	23.0(1.0)	770(30)	H110α, 3, A
G28.86+0.06 S.....	29(3)	105.3(3.0)	57.0(6.0)	701(165)	H110α, 1, A, V
IRAS 18470−0044.....	23(1)	93.4(0.2)	19.7(0.6)	479(12)	H110α, 1
	5(1)	42.9(0.8)	11.2(2.2)	64(10)	H110α, 1
Mol 75 N	(3)	...	...	...	1, N
Mol 75.....	(0.5)	...	...	...	1, N
Mol 75 S.....	13(3)	58.0(1.2)	10.3(2.9)	145(30)	H110α, 1, A
IRAS 18521+0134 N.....	12(2)	50.8(1.1)	20.2(2.3)	253(27)	H110α, 1, A, 2G
	10(2)	86.3(1.3)	21.0(3.1)	226(29)	H110α, 1, A, 2G
IRAS 18521+0134.....	7.5(0.6)	86.2(0.4)	22.4(0.9)	179(6)	H110α, 1, A, 2G
	5.2(0.6)	54.0(0.5)	18.5(1.2)	102(6)	H110α, 1, A, 2G
IRAS 18521+0134 S	17(2)	63.2(3.0)	84.0(6.0)	517(168)	H110α, 1, M, V, W
IRAS 18566+0408.....	5.0(0.7)	45.6(1.7)	38.7(4.3)	204(19)	H110α, 2
	3.5(0.7)	93.1(1.7)	17.7(3.6)	66(13)	H110α, 2
IRAS 19035+0641.....	2(1)	44.9(4.8)	42.5(9.0)	109(22)	H110α, 1, T
	6(1)	44.4(3.0)	<6.00	...	C110α, 1, T, V
IRAS 19095+0930.....	6(2)	46.3(1.4)	24.5(3.5)	166(20)	H110α, 1, A
IRDC 1923+13 N	44(3)	61.3(0.5)	25.1(1.2)	1187(47)	H110α, 1, A
	9(3)	63.5(1.3)	10.9(2.3)	102(23)	He110α, 1, T
IRDC 1923+13	7.5(0.5)	57.6(0.3)	25.0(0.9)	200(6)	H110α, 1, W
IRDC 1923+13 S.....	42(3)	59.0(0.5)	24.4(1.0)	1088(41)	H110α, 1, A
IRAS 20126+4104.....	(2)	...	...	...	1, N
MWC 349	...	...	...	...	1, O
Mol 136.....	(1)	...	...	...	1, N
Mol 138.....	2.0(0.7)	−20.3(4.4)	27.7(11.7)	59(22)	H110α, 1, 2G
	3.3(0.7)	5.2(2.1)	18.1(3.7)	65(19)	H110α, 1, 2G
Mol 145.....	(0.9)	...	...	...	1, N
Mol 145 N	(3)	...	...	...	1, N
Mol 145 S.....	(3)	...	...	...	1, N
Mol 145 E.....	(3)	...	...	...	1, N
Mol 145 W	(3)	...	...	...	1, N
Mol 148.....	(0.5)	...	...	...	1, N
NGC 7538.....	173(3)	−59.6(0.2)	32.3(0.6)	5931(92)	H110α, 1
	14(3)	−56.0(1.3)	33.0(5.1)	476(59)	He110α, 1
	9(3)	−59.7(2.0)	15.6(4.0)	149(43)	C110α, 1

TABLE 3—*Continued*

Source	S_ν (mJy)	V_{LSR} (km s^{-1})	Width (km s^{-1})	$\int S_\nu\, dv$ (mJy km s^{-1})	Notes[a]
S157	42(1)	−47.6(0.3)	23.9(0.7)	1061(19)	H110α, 1
	14(1)	−43.1(0.3)	5.2(0.7)	79(9)	C110α, 1
IRAS 23139+5939	8.4(0.8)	−46.3(0.5)	19.3(1.3)	172(10)	H110α, 1
	3.8(0.8)	−44.2(0.5)	3.6(1.1)	15(3)	C110α, 1, T
Mol 160	7(2)	−46.9(0.9)	20.4(2.3)	156(14)	H110α, 3
	12(2)	−49.5(0.2)	2.9(0.5)	36(5)	C110α, 3

NOTES.—Spectrum rms is reported as S_ν error. Other uncertainties shown in parentheses are 1 σ statistical errors from the fit. The line parameters of the central position of the three-point scans were obtained by Sewiło et al. (2004) or Araya et al. (2004b) and are reported here for completeness. In the case of the Sewiło et al. (2004) data, instead of the rms we list the reported error in the flux density measurement. (*) Possibly narrow (<3 km s^{-1}) feature superimposed on the carbon line. When the spectrum is smoothed to a channel width of 0.375 km s^{-1}, the line parameters of the C110α line are $S_\nu = 16.5$ mJy, $V_{LSR} = 17.6(0.1)$ km s^{-1}, FWHM = 1.1(0.3) km s^{-1}, $\int S_\nu\, dv = 19(4)$ mJy km s^{-1}. (1) Spectrum smoothed to a channel width of 48.8 kHz (3.0 km s^{-1}). (2) Spectrum smoothed to a channel width of 97.6 kHz (6.0 km s^{-1}). (3) Spectrum smoothed to a channel width of 12.2 kHz (0.76 km s^{-1}). (4) Spectrum smoothed to a channel width of 195.3 kHz (12.0 km s^{-1}). (5) Spectrum smoothed to a channel width of 24.4 kHz (1.5 km s^{-1}). (O) Emission at reference position. (V) Zero power width of an asymmetric or multiple peak line is presented. The reported flux density and V_{LSR} correspond to the channel with greatest emission. (A) Asymmetric line fitted with a single Gaussian profile. (B) C110α line possibly blended with He110α line. (T) Tentative detection. (M) Multipeak line. (2G) Multipeak line fitted with two Gaussian profiles. (N) No detection. (W) Red or blue wing.

[a] Unless indicated otherwise, the line parameters were obtained by Gaussian fits to the line profiles. We report the FWHM as line width.

2005 July data. The spectra were averaged and smoothed to the final channel widths reported in the footnotes of Tables 2 and 3. Line parameters were measured after subtraction of a linear baseline. In Tables 2 and 3 we report the rms and line parameters of the H_2CO and RRL observations, respectively.

2.2. *VLA Observations*

Using the VLA in the A configuration, we conducted observations of the $J_{KaKc} = 1_{11}$–1_{10} H_2CO line on 2005 January 10. We selected 10 sources whose single-dish spectra from previous Arecibo and GBT observations (Watson et al. 2003; Sewiło et al. 2004) were consistent with H_2CO emission blended with absorption. The goal of the VLA observations was to filter out extended absorption to investigate whether the complex single-dish absorption profiles were due, in part, to blended H_2CO emission. The pointing positions, central bandpass velocities, and secondary calibrators used for the VLA observations are reported in Table 1. The VLA correlator was used in the 2IF AD mode, with a bandwidth of 1.56 MHz (97.0 km s^{-1}) and 256 channels per IF (channel width of 0.38 km s^{-1}, 6.1 kHz). We observed 3C 286 as flux density calibrator and assumed a flux density of 7.52 Jy. In addition, we observed 3C 48 to check the quality of the flux density calibration.

The calibration and imaging was done using the NRAO package AIPS following standard spectral line reduction procedures. We measured flux densities of 1.27, 0.74, and 0.67 Jy for the phase calibrators J1832−105, J1820−254, and J1922+155, respectively. Using 3C 286 as flux density calibrator, we determined a flux density of 5.63 Jy for 3C 48, which is within 3% of the expected value of 5.47 Jy.

We produced H_2CO spectral cubes for all sources in our sample. In addition, we constructed *u-v* continuum data sets excluding the band edges and the channels with H_2CO detection to image the 6 cm continuum in the regions. Table 4 contains the parameters of the continuum images, and in Table 5 we list the parameters of the H_2CO 6 cm lines detected with the VLA.

3. RESULTS

In Figures 1–5 we show the results of our GBT observations, and the images and spectra from the VLA observations are shown in Figures 6–8. The most important result of this survey is the

TABLE 4

VLA 6 cm CONTINUUM IMAGES

Source	rms (mJy beam^{-1})	θ_{syn}, P.A. (arcsec, deg)	$I_{\nu,peak}$ (mJy beam^{-1})	α_{peak}(J2000.0)[a]	δ_{peak}(J2000.0)[a]	S_ν (mJy)	Size[b] (arcsec, pc)	Notes
G10.96+0.02	0.7	0.79 × 0.42, −11	38.0	18 09 39.33[2]	−19 26 28.2[3]	212(6)	3.1, 0.2	
G13.13−0.15	0.8	0.66 × 0.36, −16	...	...	...	...	...	E
G19.07−0.28	0.6	0.67 × 0.41, −06	15,5	18 26 48.88[2]	−12 26 23.9[3]	124(4)	2.7, 0.06	
	0.6	0.67 × 0.41, −06	6.2	18 26 48.65[2]	−12 26 28.6[3]	300(9)	6.0, 0.1	
G23.46−0.20[c]	0.4	0.67 × 0.42, +21	7.8	18 34 44.913[1]	−08 31 07.36[2]	11(1)	0.36, 0.01	G
G23.71−0.20	0.3	0.63 × 0.41, +01	<1.7	...	...	...	...	N
G24.68−0.16	0.5	0.60 × 0.39, −31	<2.3	...	...	...	...	N
G28.61+0.02	0.7	0.60 × 0.41, +09	10.7	18 43 28.39[2]	−03 50 19.7[2]	226(7)	4.4, ?	
G30.84−0.11	0.6	0.43 × 0.37, −09	...	...	...	...	...	E
G43.18−0.52	0.4	0.60 × 0.43, +45	2.7	19 12 08.73[2]	+08 52 08.7[3]	253(8)	5.8, 0.2	
G49.21−0.35	0.9	0.47 × 0.36, +66	...	...	...	...	...	E

NOTES.—Units of right ascension are hours, minutes, and seconds, and units of declination are degrees, arcminutes, and arcseconds. (G) Fit with a 2D Gaussian. (N) Nondetection. (E) Extended continuum region could not be imaged.

[a] For aesthetic reasons the uncertainties are shown in brackets and should be read as, e.g., $xx.xx[y] \equiv xx.xx \pm 0.0y$.

[b] For extended sources, the reported size is the geometrical average of the brightness distribution major and minor axes measured from the 3 σ contour level. We report the geometrical average of the deconvolved size for Gaussian sources.

[c] G23.46−0.20 lies within the VLA primary beam of the G23.43−0.21 observations.

TABLE 5
H_2CO 6 cm Line Parameters from VLA Observations

Source	rms (mJy beam^{-1})	$I_{\nu,\mathrm{peak}}$[a] (mJy beam^{-1})	α_{peak}(J2000.0)[b]	δ_{peak}(J2000.0)[b]	V_{LSR} (km s^{-1})	FWHM (km s^{-1})	Size[c] (arcsec, pc)	Notes
G10.96+0.02.....	5	−26	18 09 39.35[2]	−19 26 28.0[3]	20.4(0.4)	2.3(0.4)	1.5, 0.1	A
G13.13−0.15.....	12	...	...	...	...	...	...	F
G19.07−0.28.....	7	−35	18 26 48.89[2]	−12 26 24.2[3]	65.7(0.4)	3.0(0.4)	1.4, 0.03	A
G23.43−0.21.....	6	<30	...	...	...	...	...	N
G23.71−0.20.....	5	60	18 35 12.366[1]	−08 17 39.34[2]	79.2(0.4)	0.8(0.4)	<0.4, <0.02	E
G24.68−0.16.....	6	<30	...	...	...	...	...	N
G28.61+0.02.....	10	<50	...	...	...	...	...	N
G30.84−0.11.....	8	<40	...	...	...	...	...	N
G43.18−0.52.....	4	−15	19 12 08.53[2]	+08 52 08.3[3]	58.5(0.4)	0.8(0.4)	2.0, 0.06	A
G49.21−0.35.....	12	<60	...	...	...	...	...	N

Notes.—Synthesized beams (θ_{syn}) are given in Table 4. Units of right ascension are hours, minutes, and seconds, and units of declination are degrees, arcminutes, and arcseconds. (F) Absorption in the field could not be reliably imaged. (E) Emission. (N) Nondetection. (A) Extended absorption.

[a] 5 σ upper limits listed for nondetections.

[b] For aesthetic reasons the uncertainties are shown in brackets and should be read as, e.g., $xx.xx[y] \equiv xx.xx \pm 0.0y$.

[c] For extended sources, the reported size is the geometrical average of the brightness distribution major and minor axes measured from the 3 σ contour level. We report a deconvolved size limit for unresolved sources.

detection of a new H_2CO 6 cm maser region (G23.71−0.20; Fig. 6). An extensive discussion of this detection (together with additional VLA data) is presented by Araya et al. (2006a); thus, no further discussion of the detection is presented here.

We detected H_2CO 6 cm absorption lines toward 48 of the 58 sources observed. Of these 48 regions, 45 were detected with the GBT (see Table 2 and Figs. 1, 3, 4, and 5), and three were detected with the VLA (Table 5; Fig. 7). H_2CO 6 cm absorption was detected in all pointing positions of the three- and five-point scans shown in Figures 3 and 4. By comparing the line profile of the central position with the adjacent pointing positions, we find no evidence for H_2CO 6 cm emission in the 14 sources shown in Figures 3 and 4. Thus, we conclude that the multipeak H_2CO line profiles at the central positions are likely due to the superposition of different H_2CO absorption features and not due to the superposition of emission and absorption lines.

H_2CO emission from the known H_2CO maser regions NGC 7538 and IRAS 18566+0408 was detected with the GBT (see Fig. 5). Based in part on the GBT observations of IRAS 18566+0408 reported in this work, we found a rapid flarelike variability of the H_2CO maser in IRAS 18566+0408, which is discussed by Araya et al. (2007). A discussion of the variability of the NGC 7538 H_2CO maser is given in § 4.1.

Including tentative detections, we found hydrogen radio recombination line emission (H110α) toward 29 sources (Table 3; Figs. 2, 3, 4, and 5) and He110α and C110α lines toward 10 and 14 sources, respectively. Finally, 6 cm continuum emission was detected and imaged with the VLA toward five sources (Table 4; Figs. 7 and 8). We did not obtain a reliable measurement of the 6 cm radio continuum from our GBT observations.

4. DISCUSSION

4.1. *Variability of the Maser in NGC 7538 IRS1*

We detected the two main H_2CO 6 cm maser velocity components in NGC 7538 (Fig. 5). In Figure 9 we show the updated light curve of the two H_2CO maser components, which (following Hoffman et al. 2003) are referred to as components I and II. Our observations confirm the variability of component II reported by Hoffman et al. (2003). Our data also suggest that the flux density rate of change of component I is slowing over time.

Using the GBT flux density measurement, and the 2002 and 1996 flux density values of component II (Hoffman et al. 2003), we find that the flux density rate of change of component II has been $\sim$30 mJy yr^{-1}. This value is particularly interesting because the rate of change of component I between 1983 and 1995 was also $\sim$30 mJy yr^{-1} (see Fig. 9). Thus, it might be possible that the mechanism (an isolated long-term perturbation) that caused the variability of component I is the same mechanism that is causing the variability of component II, which would explain the similar variation rates. We speculate that the delay in the variability onset of the two components (approximately 14 yr) could be the time required by the perturbation to travel from component I to component II. If this were the case, we would expect an increase in the rate of change of the component II maser from $\sim$30 mJy yr^{-1} to more than $\sim$70 mJy yr^{-1} some time after 2009, just as component I showed an increase in the variability rate after 1995 (see Fig. 9).

Assuming that the time lag in the variability onset of the two components is caused by a perturbation that triggered the variability of component I in 1982 and that required 14 yr to reach component II, and assuming a distance between components I and II of 240 AU (Hoffman et al. 2003), then a disturbance due to a change in the radiation field could be ruled out because the distance difference between the two components and an external source of radiation is of the order of a few light-days. That is, if the variability had been triggered by a change in the radiation field, both components would have shown the same variability within a few days. On the other hand, the variability could have been caused by a supersonic front. For instance, assuming a distance between the two components of 240 AU (Hoffman et al. 2003), then a shock wave with a velocity of $v \sim 80$ km s^{-1} could have reached component II 14 yr after reaching component I.

To test the hypothesis that the variability of the two maser components in NGC 7538 has a common origin, we recommend a long-term monitoring program of the H_2CO masers in NGC 7538. The goal of such monitoring observations would be to check whether component II shows an increase in the variability rate after 2009 similar to the increase in the variability rate of component I after 1995.

4.2. *Extended Molecular Gas and Radio Recombination Line Emission*

As mentioned in § 3, the three- and five-point scans shown in Figures 3 and 4 were obtained to determine whether the complex H_2CO absorption profiles are consistent with H_2CO maser

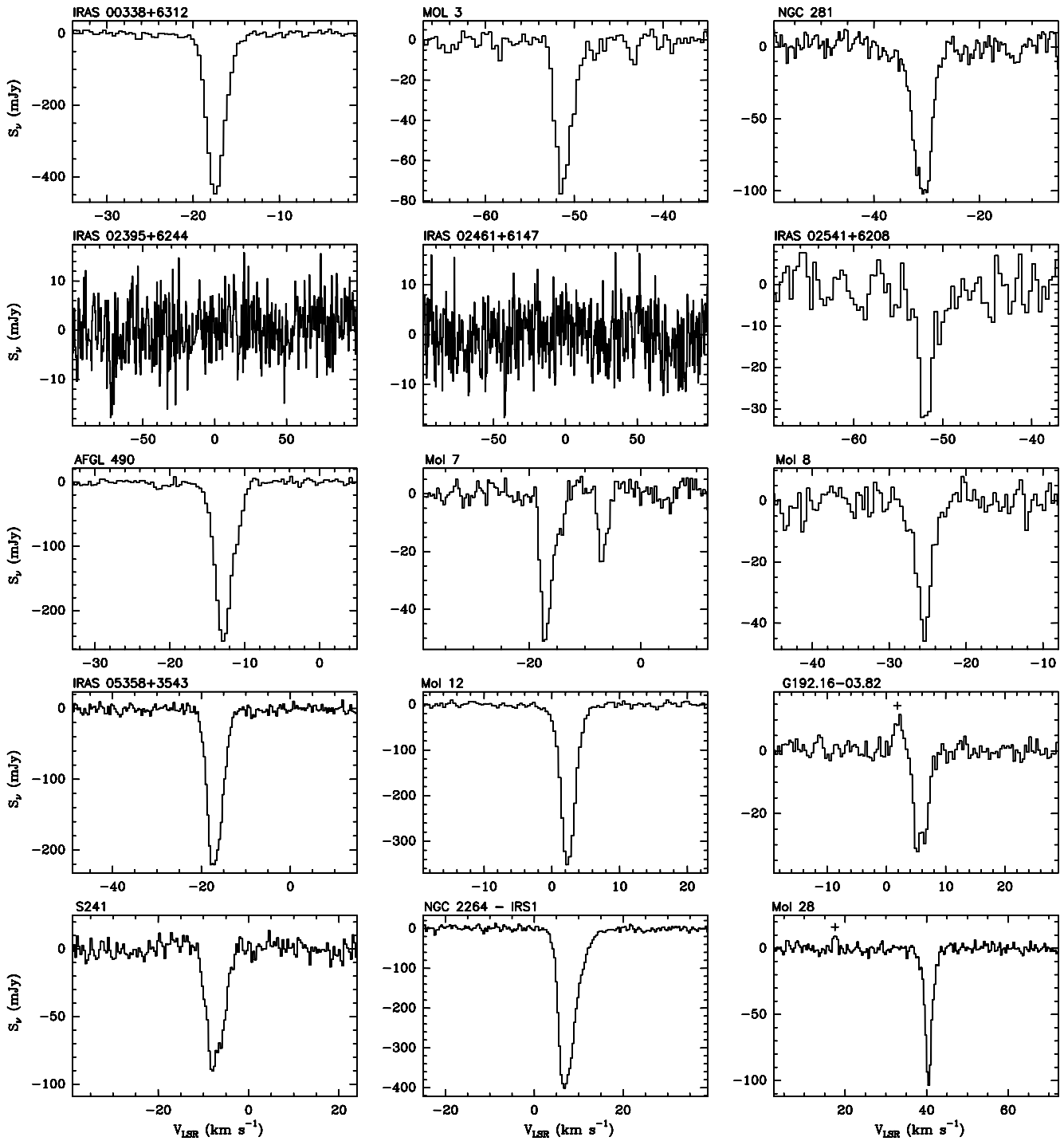

FIG. 1.—H_2CO 6 cm spectra obtained with the GBT (beam size $\sim$2.5′). We mark with a plus sign artifacts due to absorption in reference position. The spectra shown here are from single-pointing observations. Multiple-pointing spectra are shown in Figs. 3 and 4.

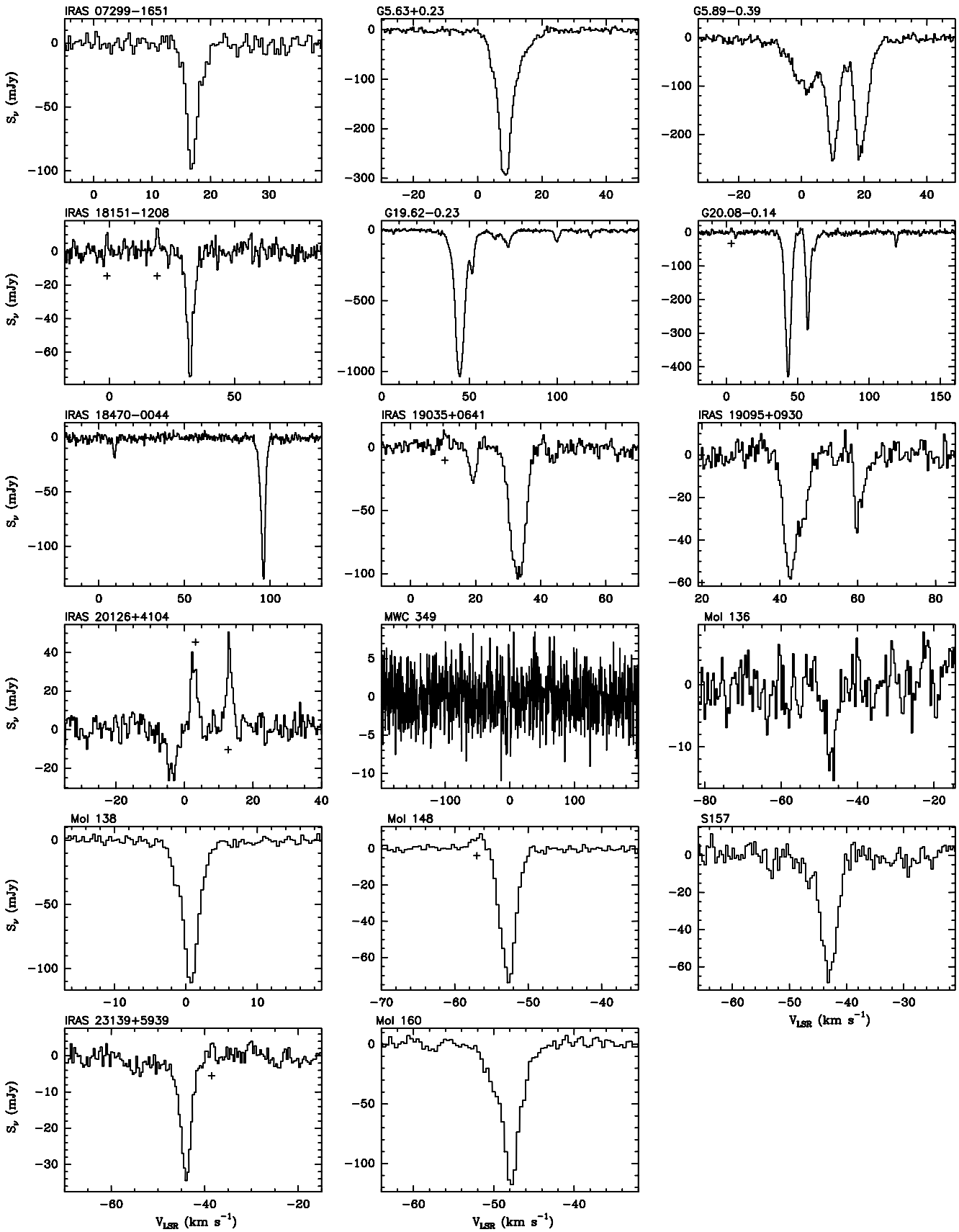

FIG. 1—*Continued*

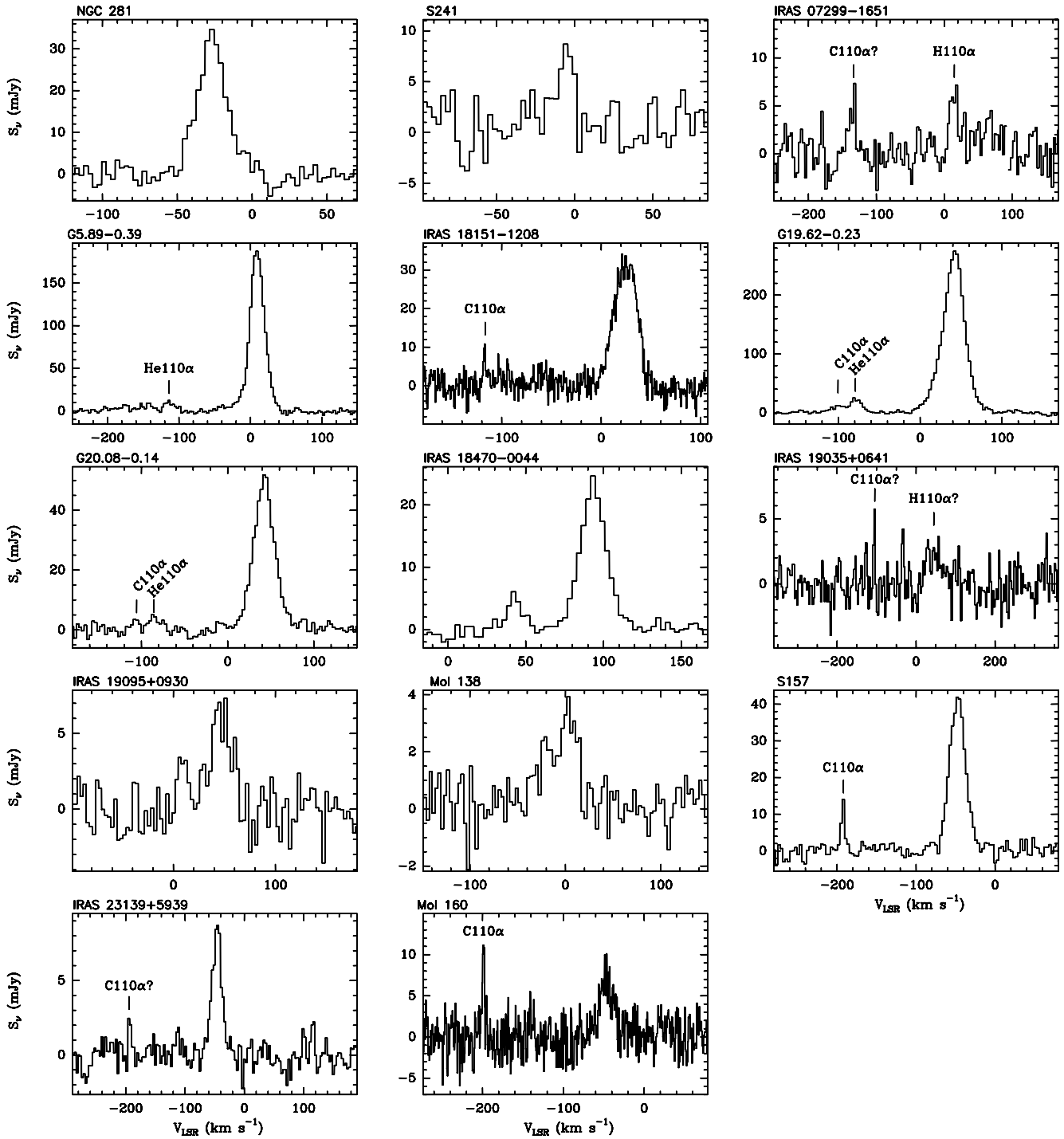

FIG. 2.—Radio recombination lines detected with the GBT (beam size ∼2.5′). The lines are H110α transitions unless otherwise indicated. The velocity scale is set with respect to the H110α transition. The He110α and C110α lines are blueshifted from the H110α line by 122.166 and 149.560 km s^{-1}, respectively (e.g., Rohlfs & Wilson 2000). We do not include the multipointing RRL detections that are shown in Figs. 3 and 4, nor the lines detected toward IRAS 18566+0408 and NGC 7538 shown in Fig. 5.

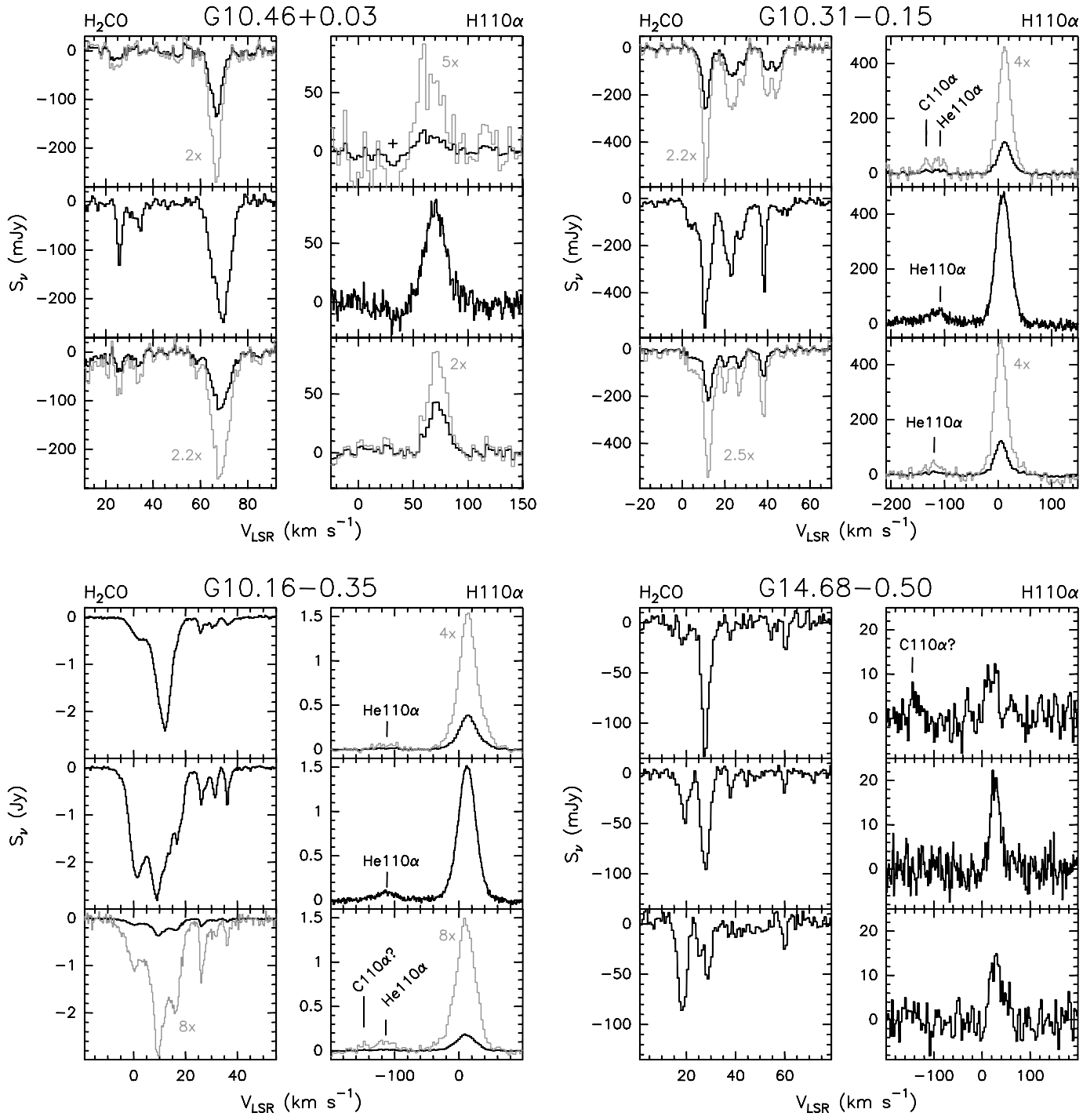

FIG. 3.—Three-point H_2CO and H110α scans toward H_2CO 6 cm emission candidates (sources in group 2 as defined in § 2.1). The reference positions of the central spectra are given in Table 1. The central position spectra of Mol 75, IRAS 18521+0134, and IRDC 1923+13 were obtained with the Arecibo Telescope (Paper I). All other central position spectra were obtained with the GBT by Sewiło et al. (2004). The top (north) and bottom (south) spectra were obtained with the GBT (beam size $\sim$2.5′) at offset positions of +2.5′ and −2.5′ from the central position (Table 1). For clarity, in some cases we rescale the data to highlight line profiles (*thin line*). We mark spurious features with a plus sign.

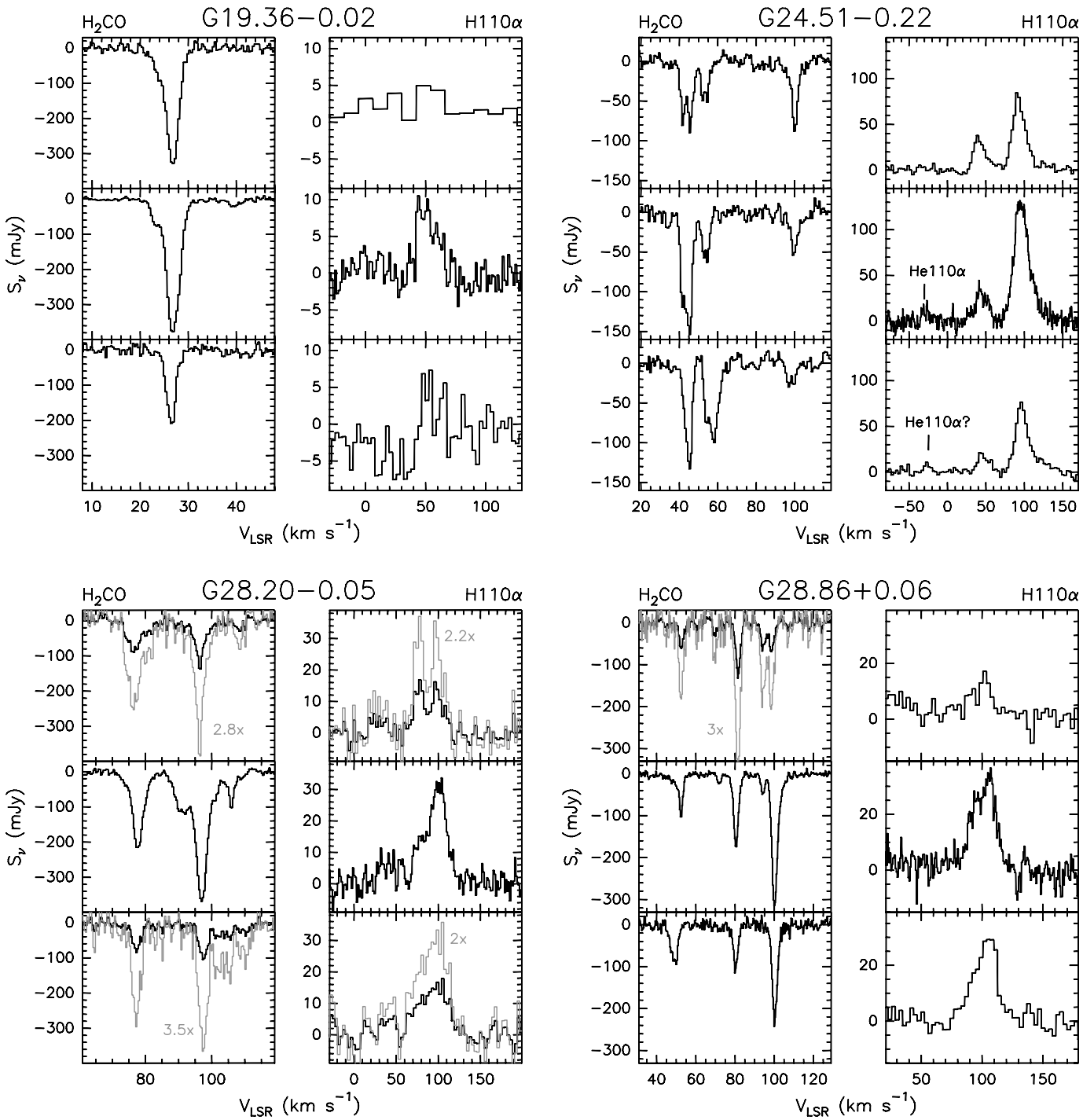

FIG. 3—*Continued*

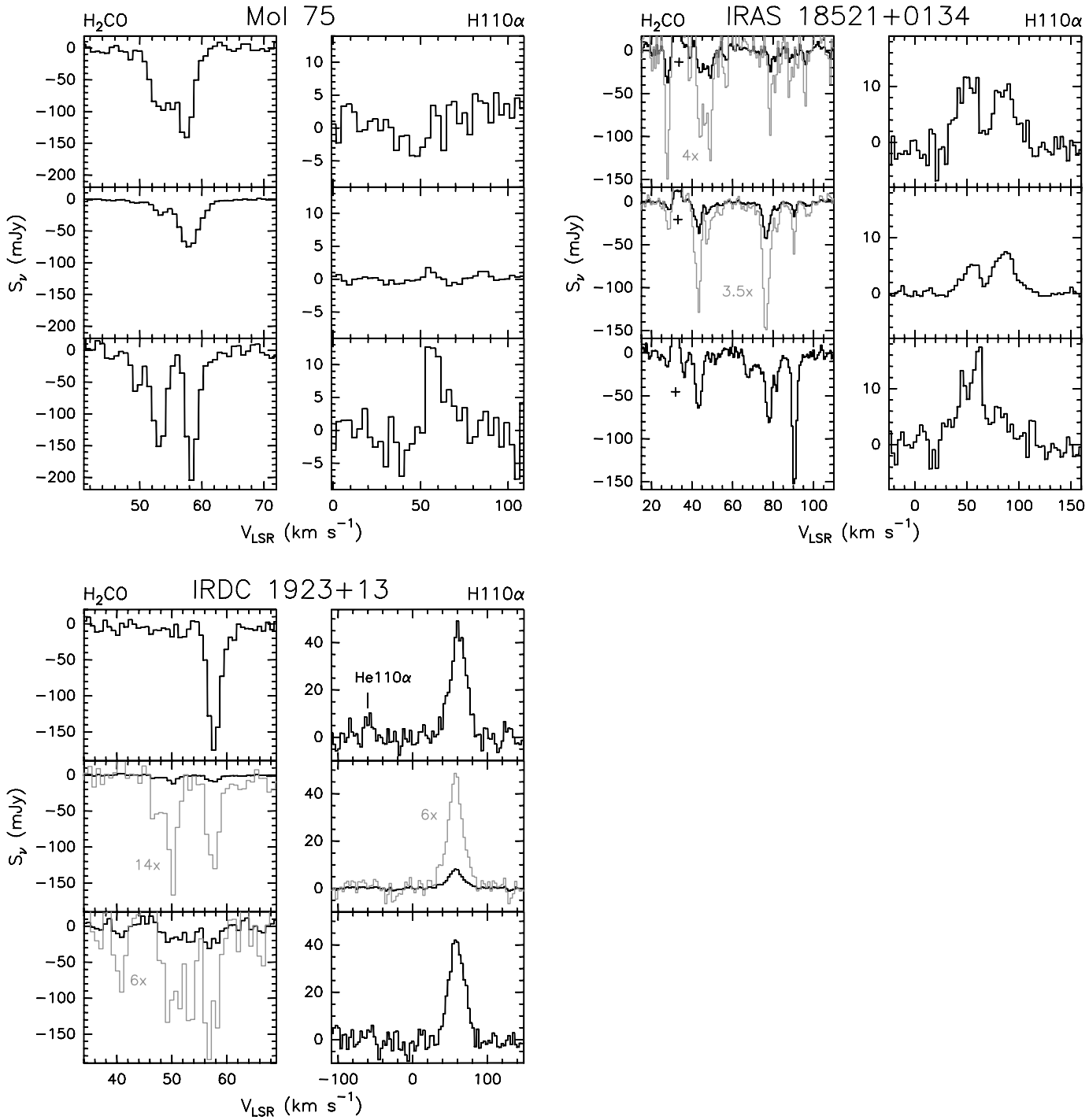

FIG. 3—*Continued*

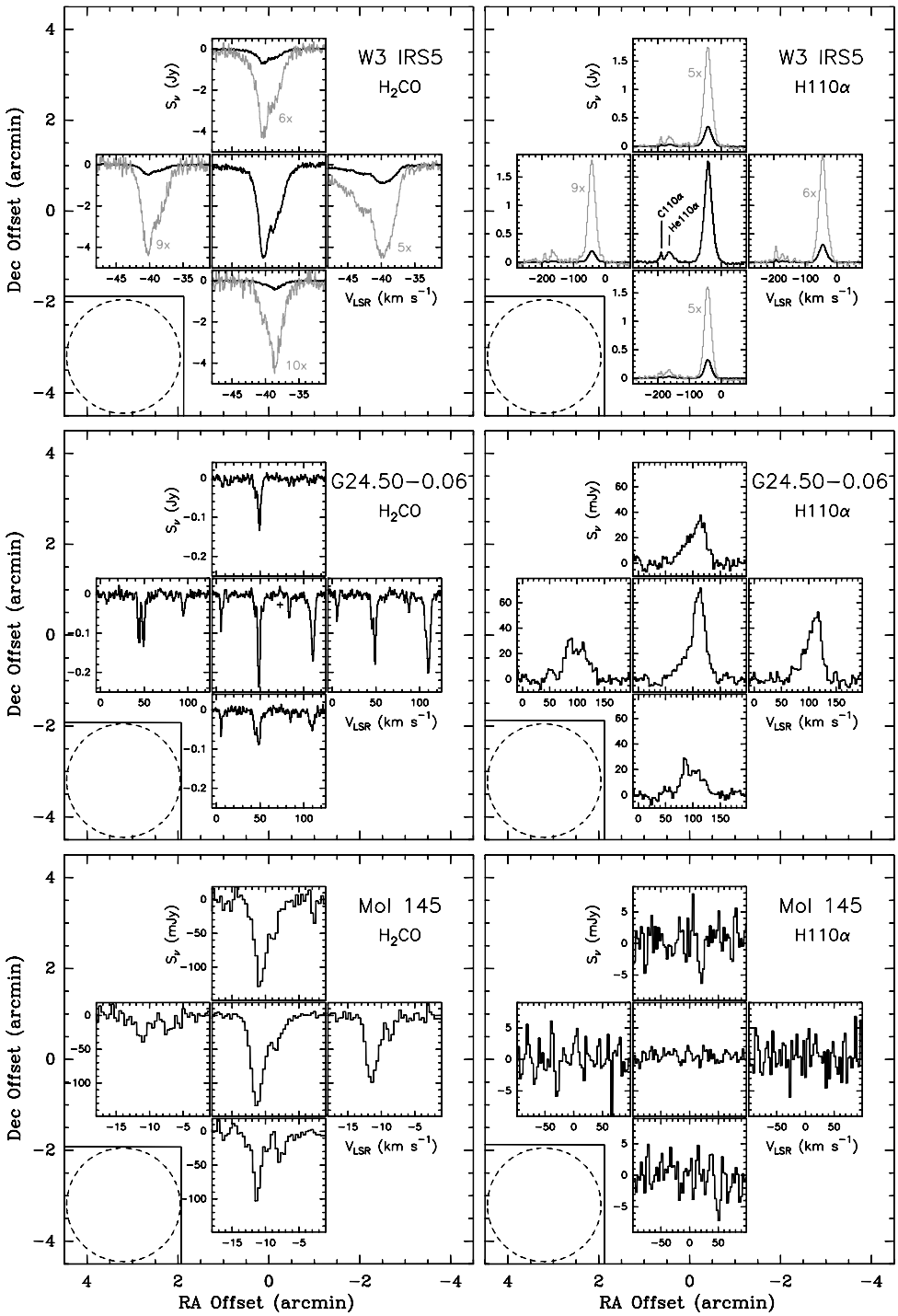

FIG. 4.—Cross scans toward W3 IRS 5, G24.50−0.06, and Mol 145 obtained with the GBT (beam size ∼2.5′). The H_2CO and the H110α spectra are shown in the left and right columns, respectively. In the case of the W3 IRS5 offset pointings, we show rescaled spectra to highlight the line profiles (*thin lines*).

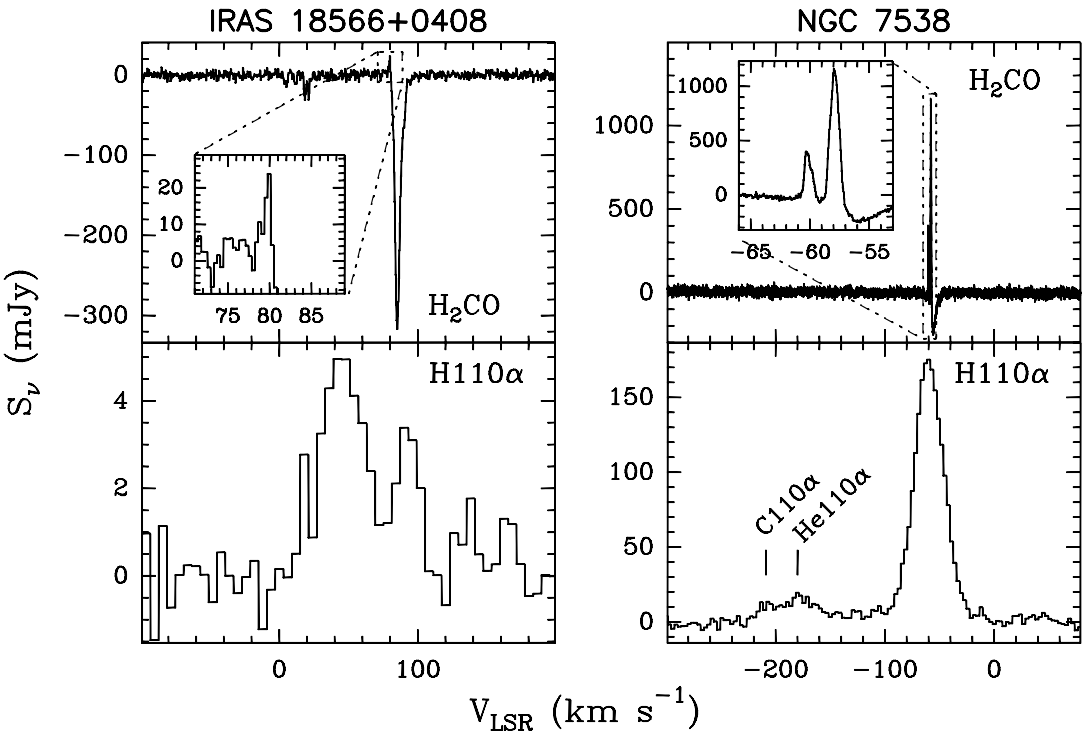

FIG. 5.—H_2CO and H110α spectra obtained with the GBT (beam size $\sim$2.5′) toward the known H_2CO 6 cm maser regions IRAS 18566+0408 and NGC 7538.

emission blended with absorption or whether they more likely arise from superposition of different absorption features. Although we did not find new candidates for H_2CO maser emission, these observations enable a study of the spatial distribution of molecular gas (traced by H_2CO absorption) and continuum emission (traced by the H110α line). Given the distances to the sources (Table 1) and the GBT beamwidth ($\sim$2.5′), the physical sizes of the three- and five-point scans shown in Figures 3 and 4 are between $\sim$6 and $\sim$30 pc (the size scale of most of the maps is $\sim$20 pc). In general, a given H_2CO absorption feature is detected toward at least two nearby pointing positions, which shows that H_2CO traces structures larger than $\sim$6 pc. Similarly, H110α emission is more extended than the GBT beam in all the sources for which the H110α line was detected at the central position of the three- and five-point scans.

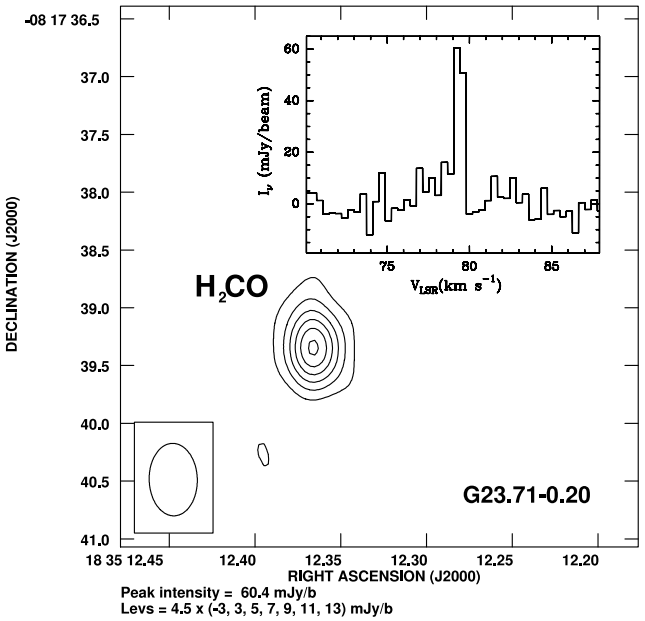

FIG. 6.—VLA detection ($\theta_{syn} \sim 0.5''$; Table 4) of H_2CO 6 cm maser emission toward G23.71−0.20 (see Araya et al. 2006a for a discussion of this detection).

To consistently address the presence of spatial gradients in the ionized gas, we selected the five sources whose H110α line profiles are well fit by a single Gaussian, i.e., W3 IRS5, G10.31−0.15, G10.16−0.35, G24.51−0.22, and IRDC 1923+13. From these sources we find monotonic H110α velocity gradients in three of the sources (G10.31−0.15, G10.16−0.35, and G24.51−0.22); i.e., the H110α peak velocity increases or decreases along the north-south direction. For three sources (W3 IRS5, G10.31−0.15, and G24.51−0.22) the maximum H110α FWHM is at the central position and also corresponds to the maximum in H110α emission. W3 IRS5 and G10.31−0.15 also show a maximum in the H_2CO line width (Table 2) toward the central position with respect to the values from the north (2.5′) and south (−2.5′) pointing offsets. The large line width of the H110α and H_2CO lines at the central positions suggests that the massive star formation process at the central positions is injecting energy into the surrounding medium, which has significantly increased the turbulence of the ionized and molecular gas (see Araya et al. 2006b for a low-mass star formation analogy).

4.3. H_2CO *Absorption as a Tool to Resolve Distance Ambiguities*

Recently Araya et al. (2002), Watson et al. (2003), and Sewiło et al. (2004) used H110α and H_2CO 6 cm observations to determine kinematic distances to massive star-forming regions in the inner Galaxy. To decide between the near and far kinematic distances, they compared H_2CO absorption features with H110α emission. If absorption was detected at velocities between the H110α velocity and the tangent point velocity, then the source was assigned a far kinematic distance. If no absorption was found

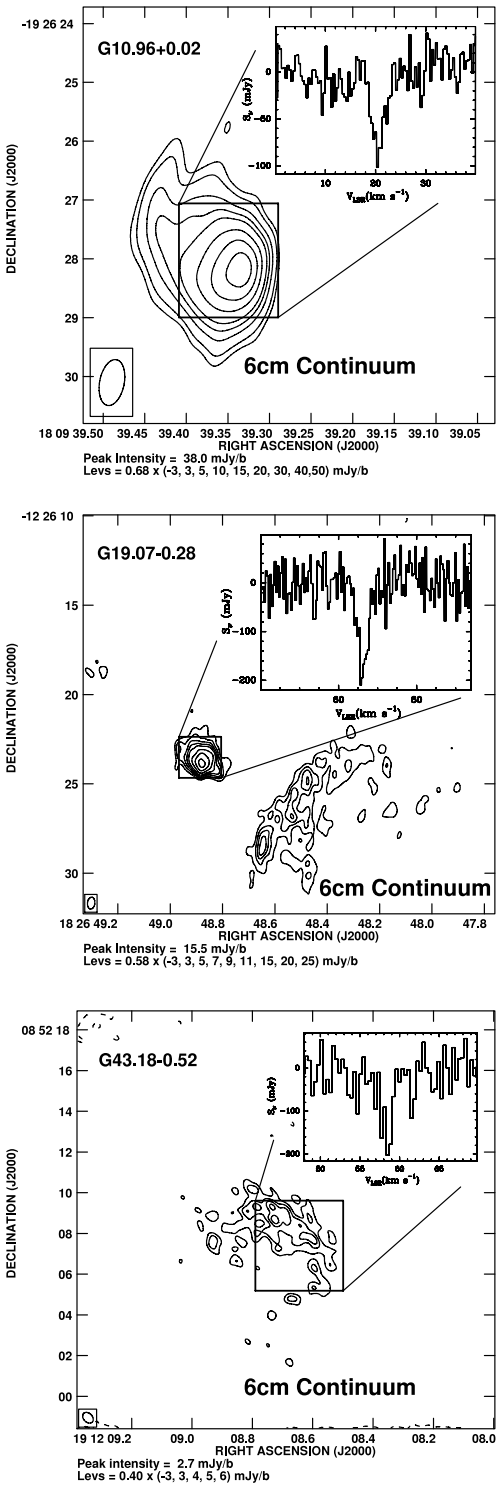

FIG. 7.—Three sources with H_2CO absorption (*insets*) and 6 cm continuum emission (*contours*) detected with the VLA ($\theta_{syn} \sim 0.5''$). The synthesized beam sizes and position angles (shown in the lower left corner) are listed in Table 4. The 6 cm radio continuum toward G43.18−0.52 was heavily resolved. G43.18−0.52 was classified as a core halo ultracompact H II region by Wood & Churchwell (1989).

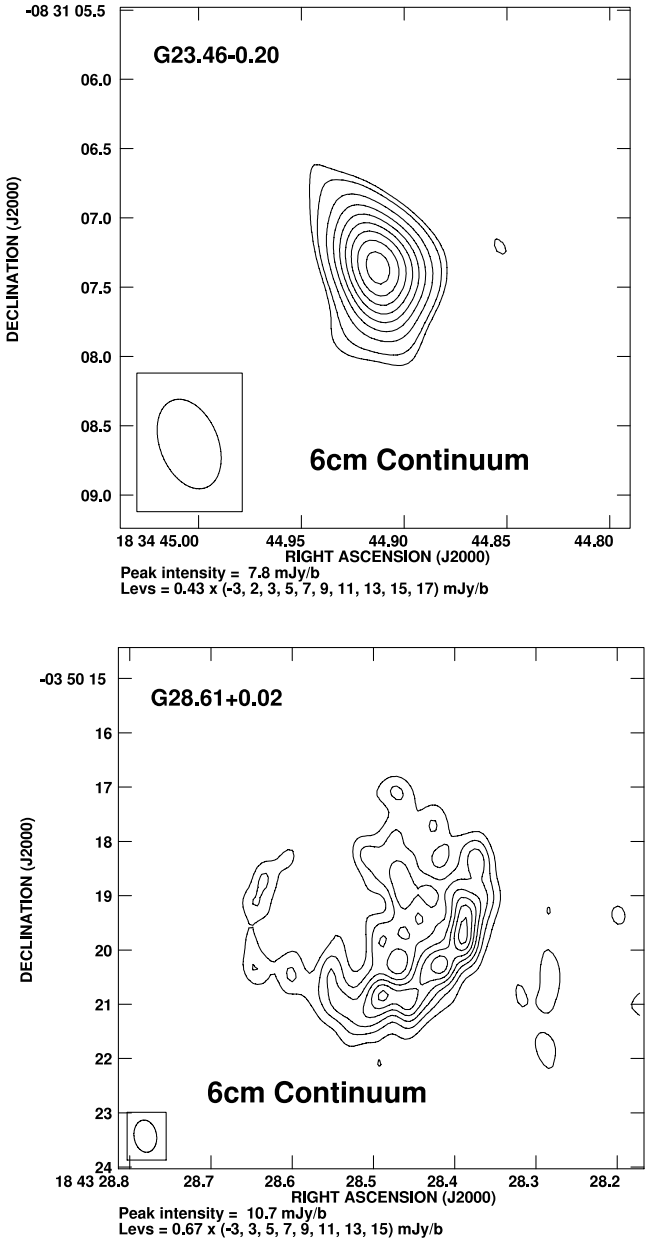

FIG. 8.—Images of the 6 cm radio continuum detected with the VLA ($\theta_{syn} \sim 0.5''$) toward G23.46−0.20 and G28.61+0.02. We did not detect H_2CO absorption toward these sources. The synthesized beam is shown in the lower left corner, and its size is given in Table 4.

between the H110α velocity and the tangent point velocity, then the near distance was preferred (for more details see Sewiło et al. 2004). The essence of the method is the assumption that all H_2CO absorption features that are not associated with the massive star-forming regions (i.e., those H_2CO features for which $|V_{LSR}^{H_2CO} - V_{LSR}^{H110\alpha}| > 10$ km s^{-1})[14] are molecular clouds in the foreground of the H II region that are observed in absorption against the radio continuum. The validity of this assumption is unclear given that the H_2CO 6 cm line can be detected in absorption against the cosmic microwave radiation (CMB) and, for sources located near the Galactic center, against the diffuse Galactic background. That is, H_2CO absorption features could come from background instead of foreground clouds with respect to the H II region. As such, this method appears not to be a conclusive test of the near-far ambiguity.

The three- and five-point scans obtained with the GBT allow us to test the hypothesis that the nonassociated H_2CO features are

[14] The choice of 10 km s^{-1} is dictated by the velocity dispersion within giant molecular clouds, which is typically less than ∼10 km s^{-1} (Sanders et al. 1985; Larson 1981).

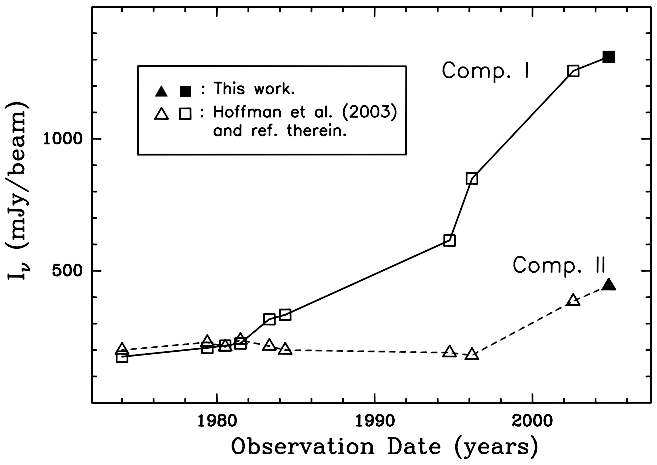

FIG. 9.—Light curve of the H_2CO 6 cm masers in NGC 7538. The filled symbols are the GBT measurements reported in this work.

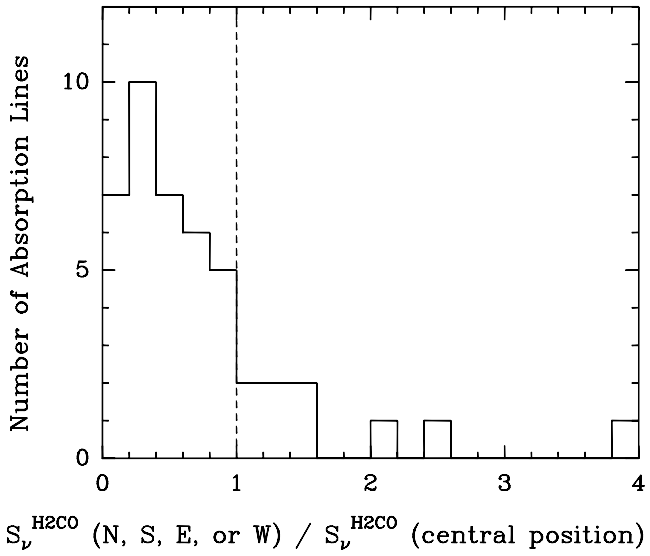

FIG. 10.—Histogram of the $S_\nu^{\rm offset}/S_\nu^{\rm central\ pointing}$ ratio of H_2CO absorption features nonassociated with the massive star formation process as traced by the H110α line (i.e., H_2CO absorption features for which $|V_{\rm LSR}^{\rm H_2CO} - V_{\rm LSR}^{\rm H110\alpha}| > 10$ km s^{-1}). In the histogram we include only H_2CO features that were detected toward the central position and toward (at least) one offset position. Most of the nonassociated H_2CO features show less flux density at offset positions in comparison with the central position where the free-free emission is greater; i.e., most of the nonassociated H_2CO features lie to the left of the dashed line. This supports the hypothesis that the nonassociated H_2CO features are observed in absorption against the radio continuum of the H II regions.

indeed foreground clouds observed in absorption against the H II region radio continuum. For this analysis we study the subsample of sources that were only observed with the GBT (i.e., excluding the sources whose central position spectra were obtained with Arecibo) and that have a single H110α emission line detected at the central position. As Figures 3 and 4 show, for these sources the maximum of the H110α line emission is always found at the central position, but H110α emission is also detected in the nearby pointing positions.

If the nonassociated H_2CO features are indeed caused by absorption against the radio continuum of the H II region, then the strongest absorption would be expected toward the central position (where the radio continuum is greatest) in comparison with the absorption detected in nearby offsets (where the radio continuum is weaker). On the other hand, if the nonassociated H_2CO features trace background clouds seen in absorption against the CMB and/or against the diffuse Galactic background, then the peak absorption should be independent of the pointing position; i.e., the absorption does not have to be stronger toward the central position.

To test whether the nonassociated H_2CO features are caused by absorption against the radio continuum from the H II region, we selected all nonassociated H_2CO absorption features that were detected toward the central position and toward at least one offset position. For each nonassociated H_2CO absorption feature we obtained the ratio between the flux density at the offset position and the flux density at the central position. Figure 10 shows the histogram of such flux density ratios. We found that approximately 80%[15] of the nonassociated absorption features detected at offset positions show smaller flux density than that of the corresponding H_2CO feature at the central position.

This result concurs with the assumption used by Araya et al. (2002), Watson et al. (2003), and Sewiło et al. (2004) that the nonassociated H_2CO features are due to absorption against the radio continuum of the H II regions. Thus, our observations support the use of H_2CO absorption as a tool to distinguish near and far kinematic distances.

The small number of nonassociated H_2CO features that show stronger absorption at offset positions with respect to the center pointing (i.e., those located to the right of the dashed line in Figure 10, hereafter referred as outliers) do not invalidate our conclusion. Some of these features could be caused by absorption against CMB and/or other unrelated sources. However, some of the outliers could still be foreground clouds observed in absorption against the H II region continuum because, as mentioned above, we detected radio recombination line emission in all offset positions for the sources used in this analysis; i.e., the radio continuum of the H II regions is extended. Thus, some of the outliers may be caused by absorption against the H II region radio continuum but show greater absorption at an offset position only due to column density gradients.

4.4. *Detection of* C110α *Lines*

The C110α line was detected toward 14 sources (including tentative detections; see Table 3 and Figs. 2, 3, and 4). The line widths (FWHM) range between 2.8 and 21.5 km s^{-1}, with a median of 9.2 km s^{-1}. The greatest line width was detected toward G19.62−0.23, and it is likely the superposition of the C110α line with one or more radio recombination lines from heavier elements. The narrowest line was detected toward IRAS 18151−1208. We find that in most cases, the narrow C110α lines (FWHM $\lesssim$ 6 km s^{-1}) are found toward sources without a He110α detection. As expected, the C110α lines are narrower than the H110α lines because of the higher mass of the carbon atom and the lower turbulence and temperature of the photodissociation regions (PDRs) from which most of the CRRL emission originates (e.g., Natta et al. 1994; Onello & Phillips 1995; Garay et al. 1998; Quireza et al. 2006). The C110α line widths (Table 3) reported in this work imply that turbulent motions in the gas must be present because the PDR kinetic temperatures obtained by assuming that the C110α FWHM is completely thermal are significantly greater than 1000 K for most sources.

In four of the sources with C110α emission (G10.31−0.15, G10.16−0.36, G14.68−0.50, and G24.50−0.06) we detected the C110α line toward an offset position and not toward the central position of the three- and five-point scans where the H110α line

[15] 80% is actually a lower limit because there are nonassociated H_2CO features detected toward the central position but *not* detected toward an offset position.

is strongest. If only single-pointing observations of these sources had been conducted, then these sources would have been reported as C110α nondetections. This result indicates that previous single-pointing surveys of carbon radio recombination line emission toward H II regions may have underestimated the number of CRRL emitters and that the presence of stronger radio continuum (where stronger stimulated emission would be expected) is not necessarily the dominant factor that determines the flux density of CRRLs in high-mass star-forming regions.

We find that the velocity difference dispersion between C110α lines and H_2CO (the rms of $V_{H_2CO} - V_{C110\alpha}$) is slightly smaller than the velocity difference dispersion between C110α and H110α lines (the rms of $V_{H110\alpha} - V_{C110\alpha}$), that is, 3 and 4.4 km s^{-1} rms, respectively (the typical error in the LSR velocity of the lines is smaller than $\sim$2 km s^{-1}; see Tables 2 and 3). This suggests that the CRRLs do not reflect the dynamics of the ionized gas but are more closely associated with the molecular material. The association between CRRLs and molecular gas toward young stellar objects has been noted before (e.g., Gómez et al. 1998), and in particular for the case of molecular gas traced by H_2CO (e.g., Roshi et al. 2006; Kantharia et al. 1998).

5. SUMMARY

We report the most extensive survey made to date exclusively focused on the search for Galactic H_2CO 6 cm maser emission. We have observed 58 sources, 48 with the Green Bank Telescope and 10 with the Very Large Array, mostly toward young regions of massive star formation. In this survey we detected the fifth H_2CO maser region in the Galaxy (G23.71$-$0.20). A detailed discussion of this detection, in addition to further VLA observations, is reported by Araya et al. (2006a).

We also observed the known H_2CO 6 cm maser sources IRAS 18566+0408 and NGC 7538 with the GBT to monitor the variability of the H_2CO masers in these regions. A discussion of the variability of the H_2CO maser in IRAS 18566+0408 (partially based on the observations reported in this paper) is presented by Araya et al. (2007). Our GBT observations of the maser in NGC 7538 confirm the variability of the blueshifted component (Hoffman et al. 2003). Based on the similar rate of change of the two maser components in NGC 7538, the variability of the two components may have the same origin. It is possible that the delay of the variability onset of both maser components could be a consequence of the distance difference between the components and the region that triggered the variability. If this is the case, the variability could not have been caused by a change in the radiation field. It seems more likely that a shock front may be the agent causing the variability of the two maser regions. Given that the redshifted maser component showed an increase in the flux density rate of change in 1996, we speculate that the blueshifted component may also show an increase in the flux density rate of change sometime after 2009. If such an increase is observed, then a common origin of the variability of the two components would be supported.

In this paper we also report line parameters of the H_2CO absorption features detected with the GBT and VLA. We detected H_2CO absorption toward 45 sources with the GBT and toward three sources with the VLA. We also detected 6 cm continuum with the VLA toward five sources. Given the versatility of the GBT correlator, we also simultaneously observed the H110α, He110α, and C110α lines toward the 48 sources. We detected H110α emission toward 29 sources, He110α toward 10 sources, and C110α line toward 14 sources (including tentative detections). In addition, we obtained three- and five-point scans toward 14 sources. We find that, in general, the H_2CO and H110α line-emitting regions are more extended than the GBT beam ($\sim$2.5′).

We checked the validity of using simultaneous H110α and H_2CO 6 cm observations to resolve the distance ambiguity of massive star-forming regions (e.g., Araya et al. 2002; Sewiło et al. 2004). For the sources with three- and five-point scans, and using the H_2CO 6 cm absorption features nonassociated with the massive star-forming regions (i.e., the H_2CO absorption features such that $|V_{H_2CO} - V_{H110\alpha}| > 10$ km s^{-1}), we find that most of the absorption features are weaker at pointing positions offset from the central position. Given that the maximum of radio continuum (as traced by the H110α line) is found at the central position, the weaker H_2CO absorption detected around the central position suggests that the H_2CO features nonassociated with the massive star-forming regions are observed in absorption against the radio continuum of the H II regions. The premise that all H_2CO features are detected in absorption toward the radio continuum of the H II regions is the hypothesis to resolve distance ambiguities as done by Araya et al. (2002), Watson et al. (2003), and Sewiło et al. (2004). Thus, our results support the use of H110α and H_2CO observations to resolve distance ambiguities.

We find that the C110α emission peak position frequently does not coincide with the H110α emission peak, which suggests that previous single-dish surveys for CRRLs may have underestimated the number of regions with CRRL emission. The sources with C110α detection reported in this work are good candidates for future multitransition CRRL observations to study the properties of photodissociated regions and to address the possibility of pressure confinement as the solution of the lifetime problem of ultracompact H II regions (e.g., Roshi et al. 2005a, 2005b).

Support for this work was provided by the NSF through award GSSP 05-0006 from the NRAO. E. A. thanks Frank Ghigo, Ron Maddalena, and Dana Balser for help during the observations and Carl Bignell for scheduling the 2004 October observations as a backup project. E. A. is supported by a NRAO predoctoral fellowship. We thank an anonymous referee for comments that improved the manuscript. P. H. acknowledges support from NSF grant AST 04-54665. H. L. was supported by a postdoctoral stipend from the German Max Planck Society. L. O. was supported in part by the Puerto Rico Space Grant Consortium. This research has made use of the SIMBAD database, operated at CDS, Strasbourg, France; NASA's Astrophysics Data System; and the NASA/IPAC Extragalactic Database (NED), which is operated by the Jet Propulsion Laboratory, California Institute of Technology, under contract with NASA.

Facilities: GBT (C-band receiver), VLA (A configuration)

REFERENCES

Araya, E., Baan, W. A., & Hofner, P. 2004a, ApJS, 154, 541
Araya, E., Hofner, P., Churchwell, E., & Kurtz, S. 2002, ApJS, 138, 63
Araya, E., Hofner, P., Goss, W. M., Kurtz, S., Linz, H., & Olmi, L. 2006a, ApJ, 643, L33
Araya, E., Hofner, P., Kurtz, S., Bronfman, L., & DeDeo, S. 2005a, ApJS, 157, 279
Araya, E., Hofner, P., Kurtz, S., Linz, H., Olmi, L., Sewiło, M., Watson, C., & Churchwell, E. 2005b, ApJ, 618, 339
Araya, E., Hofner, P., Linz, H., Sewiło, M., Watson, C., Churchwell, E., Olmi, L., & Kurtz, S. 2004b, ApJS, 154, 579 (Paper I)
Araya, E., Hofner, P., Olmi, L., Kurtz, S., & Linz, H. 2006b, AJ, 132, 1851

Araya, E., Hofner, P., Sewiło, M., Linz, H., Kurtz, S., Olmi, L., Watson, C., & Churchwell, E. 2007, ApJ, 654, L95
Beuther, H., Schilke, P., Menten, K. M., Motte, F., Sridharan, T. K., & Wyrowski, F. 2002, ApJ, 566, 945
Cesaroni, R., Felli, M., Testi, L., Walmsley, C. M., & Olmi, L. 1997, A&A, 325, 725
Claussen, M. J., Gaume, R. A., Johnston, K. J., & Wilson, T. L. 1994, ApJ, 424, L41
Codella, C., Palumbo, G. G. C., Pareschi, G., Scappini, F., Caselli, P., & Attolini, M. R. 1995, MNRAS, 276, 57
Danchi, W. C., Tuthill, P. G., & Monnier, J. D. 2001, ApJ, 562, 440
Downes, D., & Wilson, T. L. 1974, ApJ, 191, L77
Downes, D., Wilson, T. L., Bieging, J., & Wink, J. 1980, A&AS, 40, 379
Fiebig, D., Duschl, W. J., Menten, K. M., & Tscharnuter, W. M. 1996, A&A, 310, 199
Garay, G., Gómez, Y., Lizano, S., & Brown, R. L. 1998, ApJ, 501, 699
Gómez, Y., Lebrón, M., Rodríguez, L. F., Garay, G., Lizano, S., Escalante, V., & Cantó, J. 1998, ApJ, 503, 297
Gordon, M. A., & Sorochenko, R. L. 2002, Radio Recombination Lines: Their Physics and Astronomical Applications (1st ed.; Dordrecht: Kluwer)
Henning, T., Cesaroni, R., Walmsley, M., & Pfau, W. 1992, A&AS, 93, 525
Henning, Th., Martin, K., Reimann, H.-G., Launhardt, R., Leisawitz, D., & Zinnecker, H. 1994, A&A, 288, 282
Hoffman, I. M., Goss, W. M., Palmer, P., & Richards, A. M. S. 2003, ApJ, 598, 1061
Kantharia, N. G., Anantharamaiah, K. R., & Goss, W. M. 1998, ApJ, 504, 375
Kim, K.-T., & Koo, B.-C. 2001, ApJ, 549, 979
Kurtz, S., Churchwell, E., & Wood, D. O. S. 1994, ApJS, 91, 659
Kurtz, S., Hofner, P., & Vargas, C. 2004, ApJS, 155, 149
Israel, F. P. 1980, AJ, 85, 1612
Lada, C. J., & Lada, E. A. 2003, ARA&A, 41, 57
Larson, R. B. 1981, MNRAS, 194, 809
Mehringer, D. M., Goss, W. M., & Palmer, P. 1995, ApJ, 452, 304
Molinari, S., Brand, J., Cesaroni, R., & Palla, F. 1996, A&A, 308, 573
Natta, A., Walmsley, C. M., & Tielens, A. G. G. M. 1994, ApJ, 428, 209
Onello, J. S., & Phillips, J. A. 1995, ApJ, 448, 727
Palagi, F., Cesaroni, R., Comoretto, G., Felli, M., & Natale, V. 1993, A&AS, 101, 153
Pratap, P., Menten, K. M., & Snyder, L. E. 1994, ApJ, 430, L129
Quireza, C., Rood, R. T., Balser, D. S., & Bania, T. M. 2006, ApJS, 165, 338
Rohlfs, K., & Wilson, T. L. 2000, Tools of Radio Astronomy (3rd ed.; Berlin: Springer)
Roshi, D. A., Balser, D. S., Bania, T. M., Goss, W. M., & De Pree, C. G. 2005a, ApJ, 625, 181
Roshi, D. A., De Pree, C. G., Goss, W. M., & Anantharamaiah, K. R. 2006, ApJ, 644, 279
Roshi, D. A., Goss, W. M., Anantharamaiah, K. R., & Jeyakumar, S. 2005b, ApJ, 626, 253
Rudolph, A. L., Brand, J., de Geus, E. J., & Wouterloot, J. G. A. 1996, ApJ, 458, 653
Sanders, D. B., Scoville, N. Z., & Solomon, P. M. 1985, ApJ, 289, 373
Schreyer, K., Helmich, F. P., van Dishoeck, E. F., & Henning, Th. 1997, A&A, 326, 347
Sewiło, M., Watson, C., Araya, E., Churchwell, E., Hofner, P., & Kurtz, S. 2004, ApJS, 154, 553
Shepherd, D. S., Borders, T., Claussen, M., Shirley, Y., & Kurtz, S. 2004, ApJ, 614, 211
Snyder, L. E., Buhl, D., Zuckerman, B., & Palmer, P. 1969, Phys. Rev. Lett., 22, 679
Sridharan, T. K., Beuther, H., Schilke, P., Menten, K. M., & Wyrowski, F. 2002, ApJ, 566, 931
Tafoya, D., Gómez, Y., & Rodríguez, L. F. 2004, ApJ, 610, 827
Tucker, K. D., Tomasevich, G. R., & Thaddeus, P. 1970, ApJ, 161, L153
Vallée, J. P. 1987, Ap&SS, 139, 129
Watson, C., Araya, E., Sewiło, M., Churchwell, E., Hofner, P., & Kurtz, S. 2003, ApJ, 587, 714
Whiteoak, J. B., & Gardner, F. F. 1983, MNRAS, 205, 27P
Wood, D. O. S., & Churchwell, E. 1989, ApJS, 69, 831
Young, K. E., Lee, J.-E., Evans, N. J., II, Goldsmith, P. F., & Doty, S. D. 2004, ApJ, 614, 252
Zuckerman, B., Palmer, P., & Rickard, L. J. 1975, ApJ, 197, 571